Opposing Tumor-Promoting and -Suppressive Functions of Rictor/mTORC2 Signaling in Adult Glioma and Pediatric SHH Medulloblastoma

Seçkin Akgül[1,2,4,5,6,14,15], **Yinghua Li**[4,5,6,15], **Siyuan Zheng**[7], **Marcel Kool**[8,9], **Daniel M. Treisman**[1,2,4,5,6], **Chaoyang Li**[4,5,6], **Yuan Wang**[4,5,6], **Susanne Gröbner**[8,9], **Tsuneo Ikenoue**[10], **Yiping Shen**[11], **Sandra Camelo-Piragua**[3], **Gerald Tomasek**[2], **Sebastian Stark**[8,9], **Vinay Guduguntla**[2], **James F. Gusella**[11], **Kun-Liang Guan**[10], **Stefan M. Pfister**[8,9,12], **Roel G.W. Verhaak**[13], and **Yuan Zhu**[1,2,4,5,6,16,*]

[1]Cellular and Molecular Biology Graduate Program, University of Michigan Medical School, Ann Arbor, MI 48109, USA

[2]Department of Internal Medicine, University of Michigan Medical School, Ann Arbor, MI 48109, USA

[3]Department of Pathology, University of Michigan Medical School, Ann Arbor, MI 48109, USA

[4]Gilbert Family Neurofibromatosis Institute, Children's National Medical Center, Washington, DC 20010, USA

[5]Center for Cancer and Immunology Research, Children's National Medical Center, Washington, DC 20010, USA

[6]Center for Neuroscience Research, Children's National Medical Center, Washington, DC 20010, USA

[7]Greehey Children's Cancer Research Institute, The University of Texas Health Science Center at San Antonio, San Antonio, TX 78229, USA

[8]Hopp Children's Cancer Center at the NCT Heidelberg (KiTZ), 69120 Heidelberg, Germany

[9]Division of Pediatric Neurooncology, German Cancer Research Center (DKFZ) and German Cancer Consortium (DKTK), 69120 Heidelberg, Germany

*Correspondence: yzhu@childrensnational.org.

[10]Department of Pharmacology and Moores Cancer Center, University of California, San Diego, La Jolla, CA 92093, USA

[11]Center for Genomic Medicine, Massachusetts General Hospital, Harvard Medical School, Boston, MA 02114, USA

[12]Department of Hematology and Oncology, Heidelberg University Hospital, 69120 Heidelberg, Germany

[13]Jackson Laboratory for Genomic Medicine, Farmington, CT 06032, USA

[14]Sid Faithfull Brain Cancer Research Laboratory, Cell & Molecular Biology Department, QIMR Berghofer Medical Research Institute, Brisbane 4006, Australia

[15]These authors contributed equally

[16]Lead Contact

SUMMARY

Most human cancers arise from stem and progenitor cells by the sequential accumulation of genetic and epigenetic alterations, while cancer modeling typically requires simultaneous multiple oncogenic events. Here, we show that a single *p53* mutation, despite causing no defect in the mouse brain, promoted neural stem and progenitor cells to spontaneously accumulate oncogenic alterations, including loss of multiple chromosomal (chr) regions syntenic to human chr10 containing *Pten*, forming malignant gliomas with PI3K/Akt activation. Rictor/mTORC2 loss inhibited Akt signaling, greatly delaying and reducing glioma formation by suppressing glioma precursors within the subventricular zone stem cell niche. Rictor/mTORC2 loss delayed timely differentiation of granule cell precursors (GCPs) during cerebellar development, promoting sustained GCP proliferation and medulloblastoma formation, which recapitulated critical features of *TP53* mutant sonic hedgehog (SHH) medulloblastomas with *GLI2* and/or *N-MYC* amplification. Our study demonstrates that Rictor/mTORC2 has opposing functions in neural stem cells and GCPs in the adult and the developing brain, promoting malignant gliomas and suppressing SHH-medulloblastoma formation, respectively.

In Brief

Hyperactivation of PI3K/AKT signaling is frequently observed in adult glioblastomas (GBMs), whereas sonic hedgehog-subgroup medulloblastomas (SHH-MBs) in children rarely exhibit AKT activation. Using a genetically engineered mouse model of malignant brain tumor, Akgül et al. show that Rictor/mTORC2 loss inhibits Akt signaling, which delays *p53*-mutant-driven malignant gliomas, while promoting SHH-MBs.

Graphical Abstract

Neural stem/progenitor cells in the SVZ niche

Malignant gliomas/GBMs

Granule cell precursors (GCPs)

SHH-Medulloblastomas
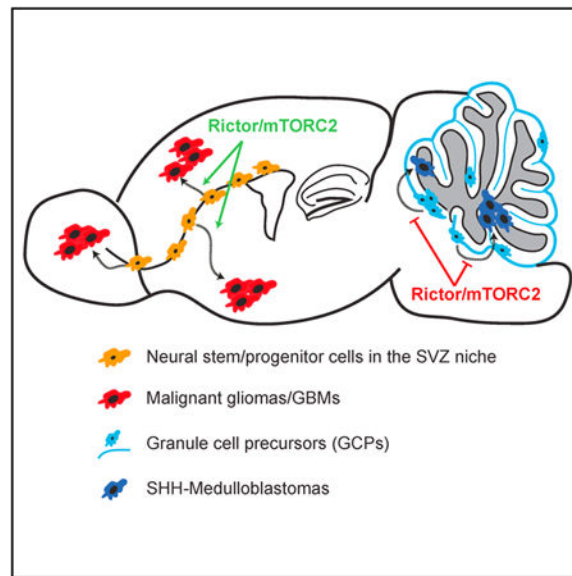
INTRODUCTION

More than 90% of human glioblastomas (GBMs) are primary or *de novo* GBMs with no evidence of pre-existing lower-grade lesions (Louis et al., 2016). Rapid clinical course presents a tremendous challenge in defining the temporal sequence and functional outcomes of accumulating each of the oncogenic driver alterations in neural stem or progenitor cells during the development of primary GBMs. One recent study using a bioinformatics approach inferred that most somatic *TP53* mutations (90.5%) were clonal, occurring in every tumor cell of the GBM samples analyzed and thus representing one of the early founding events in *TP53* mutant primary GBMs (Kim et al., 2015). Moreover, individuals with Li-Fraumeni syndrome (LFS) carrying germline *TP53* mutations have increased risks of developing malignant gliomas and GBMs as well as medulloblastomas (MBs), the most common malignant brain tumor in children (Louis et al., 2016). Consistent with an initiating role of *TP53* mutations in human brain tumorigenesis, conditional inactivation of *p53* in the mouse brain induces malignant gliomas and GBMs and, less frequently, MBs (Wang et al., 2009; Zheng et al., 2008). Both clinical observations and mouse modeling studies suggest that p53 plays a critical role in the initiation of both GBMs and MBs. However, loss of *p53* alone leads to little or no effect on the mouse brain during development or in adulthood (Chow et al., 2011; Shingu et al., 2017; Wang et al., 2009; Zheng et al., 2008). Therefore, this conditional neural-specific *p53*-mutant model must accumulate cooperating oncogenic alterations in cells with sustained proliferative potentials—neural stem or progenitor cells— to drive malignant transformation in the brain (Ihrie and Alvarez-Buylla, 2011; Wang et al., 2009, 2012).

Loss of the long arm of chromosome 10 (chr10q) appears to be a common mechanism, occurring in almost all primary GBMs, but less frequently in secondary GBMs that arise from pre-existing lower-grade gliomas harboring isocitrate dehydrogenase 1 (*IDH*) mutations (Brennan et al., 2013; Louis et al., 2016; Sturm et al., 2014). Although loss of a

relatively large region of chr10q suggests the existence of multiple tumor-suppressor genes, the most studied is the *PTEN* tumor suppressor, which negatively regulates the phosphoinositide 3-kinase (PI3K) signaling pathway (Janku et al., 2018; Ozawa et al., 2014). Loss of *PTEN* in chr10q is consistent with the observation that most GBMs in humans (>80%) exhibit activation of AKT signaling, the best characterized downstream effector of the PI3K/PTEN signaling pathway (Janku et al., 2018; Wang et al., 2004). AKT requires two phosphorylation events for full activation: (1) PDK1 phosphorylates AKT at threonine-308 (AKT^{Thr308}) and (2) the mechanistic target of rapamycin complex 2 (mTORC2) is the major kinase that phosphorylates AKT at serine-473 (AKT^{Ser473}) (Janku et al., 2018; Laplante and Sabatini, 2012; Wu et al., 2014). Given its critical functions on metabolic reprogramming and drug resistance, mTORC2 has recently been emerging as an attractive therapeutic target for human GBMs (Masui et al., 2013, 2015; Wu et al., 2014). It has been shown that loss of *RICTOR/Rictor*, an essential subunit of mTORC2, is sufficient to inhibit phosphorylation of AKT/Akt at serine-473, inactivate AKT/Akt, and, consequently, prevent tumor formation in several *Pten*-loss-driven mouse cancer models, including prostate cancer and leukemia, as well as in a *Drosophila* glioma model (Guertin et al., 2009; Kalaitzidis et al., 2012; Magee et al., 2012; Read et al., 2009). However, whether Rictor/mTORC2 signaling in neural stem or progenitor cells is required for the formation of primary GBM remains to be determined.

In contrast to GBMs, mutations in *PTEN* or other components of the PI3K signaling pathway are rare in MBs, and more important, almost no phosphorylated AKT^{Ser473} (<5%) was observed in pediatric sonic hedgehog-MBs (SHH-MBs), the only MB subtype observed in individuals with LFS (Kool et al., 2014; Northcott et al., 2012). These intriguing observations raise the possibility of whether mTORC2/AKT signaling has opposing effects on the formation of *TP53* mutant primary GBMs versus SHH-MBs.

RESULTS

p53-Mutant GEM Gliomas Spontaneously Acquire Common Genomic Alterations Observed in Human Primary GBMs

Using a Cre transgenic line controlled by the human glial fibrillary acidic protein promoter (hGFAP-cre), we previously developed three genetically engineered mouse (GEM) glioma models driven by a conditional in-frame deletion of exons 5 and 6 of the *p53* gene (1) alone (hGFAP-cre;$p53^{E5-6/E5-6}$) or (2) in combination with a germline heterozygous neurofibromatosis type 1 (*Nf1*) mutation (hGFAP-cre;$p53^{E5-6/E5-6}$;$Nf1^{+/-}$), and (3) a germline *p53* null and a conditional *Nf1* mutation on the same chromosome (hGFAP-cre;*cis*-$p53^{+/-}$;$Nf1^{+/flox}$) (Wang et al., 2009, 2012; Zhu et al., 2005). All three GEM models frequently developed malignant gliomas, which harbor homozygous *p53* deletion with or without additionally targeted *Nf1* deletion, hereafter referred to as $p53^{5-6/5\mp6}$, $p53^{5-6/5-6}Nf1^{-/-}$ and $p53^{-/-}Nf1^{-/-}$, respectively. These malignant gliomas exhibited critical histopathological characteristics of human high-grade gliomas (grades III and IV), including nuclear atypia and frequent mitotic figures, with approximately 40% showing necrosis and/or microvascular proliferation, the diagnostic features of human GBM (Louis et al., 2016; Wang et al., 2009; Zhu et al., 2005).

The gene expression profiles of all but two of the $p53^{-/-}Nf1^{-/-}$ malignant gliomas exhibited a dominant proneural signature of human GBMs (Figure 1A) (Verhaak et al., 2010). The two exceptions with a classical signature uniquely exhibited *EGFR* amplification on chr11 (human chr7), similar to most of the human classical GBMs with *EGFR* alterations (Figures 1A and S1A–S1C) (Verhaak et al., 2010). Consistent with human proneural GBMs, all of the GEM proneural gliomas exhibited the gene expression profile that is similar to oligodendrocyte precursor cells (OPCs), which is characterized by high expression of *Olig2* and *Ascl1* (Figure 1B; data not shown) (Verhaak et al., 2010). Sanger sequencing did not reveal somatic mutations of *Idh1* or *Idh2* in these GEM gliomas (n = 7). The gene expression profiles of these gliomas did not consistently resemble *IDH* mutant GBMs with a hypermethylated phenotype or glioma CpG island methylated phenotype (G-CIMP) (Figure 1A) (Baysan et al., 2012; Noushmehr et al., 2010; Ozawa et al., 2014). Together, these results demonstrate that *p53*- and *p53/Nf1*-mutant-driven malignant gliomas genetically and molecularly resemble the proneural subtype of *IDH*-wild-type (*IDH*-WT) primary GBMs, but not *IDH* mutant G-CIMP+ secondary GBMs in humans.

To determine oncogenic driving events during *p53*- and *p53/Nf1*-mutant-driven gliomagenesis, we analyzed the copy-number alterations (CNAs) in a total of 23 malignant gliomas and GBMs. We applied Genomic Identification of Significant Targets in Cancer (GISTIC) analysis, a *de facto* community standard for characterizing local and broad CNAs in human cancers (Mermel et al., 2011). We found that both GEM *p53*-mutant gliomas and human *TP53*-mutant GBMs exhibited significantly fewer amplifications than deletions (false discovery rate [FDR] 0.25) (Figures 1C, 1D, S1D, and S1E). In GEM gliomas, approximately 1% and 16% of the genome (excluding the sex chromosome) was affected by amplifications and deletions, respectively. This pattern is remarkably similar to that observed in human *TP53* mutant *IDH*-WT GBMs—1% and 12% of the genome affected by amplifications and deletions, respectively. All 17 amplification peaks identified in GEM gliomas across chr4, −6, −7, −12, and −14 were focal (14/17 <2 MBs), a pattern reminiscent of human GBMs (Figure 1C; Table S1) (Brennan et al., 2013). Cross-referencing with human data, we found a peak in chr6 syntenic to human chr7, the most frequently gained chromosome in human *IDH*-WT but not *IDH* mutant GBMs (Figures 1C, S1A, and S1D). The chr6 amplicon encompassed *Met*, amplified in three cases. Other significant oncogenes in the amplification peaks included *Ccnd1* and *Ccnd2* (Figure 1C; Table S1). Of note, GISTIC analysis did not identify a peak centering on *Egfr*, which is also syntenic to human chr7, but it was amplified in only two cases without *Met* amplification and identified by a targeted approach (Figures S1A–S1C). These results suggest that individual GEM p53-mutant gliomas acquire different oncogenic alterations, including *Met* or *Egfr*, driving malignant transformation following *p53* inactivation (Figure S1B).

Deletions in these GEM gliomas were largely contributed by broad losses of chr7, −9, and −19 (Figures 1D, S1D, and S1E). Because mouse and human chromosomes are often not syntenic, loss of chr9 was deleted in 13/23 GEM gliomas (57%) but mapped to multiple human chromosomal regions, including chr11q, −19p, −15q, −6q, and −3. Among them, chr11q was deleted in 30% of human GBMs, and other syntenic regions were also deleted, but less frequently (Brennan et al., 2013). Loss of chr10q, the most frequent broad event found in >90% of *IDH*-WT GBMs, is mapped into multiple mouse chromosomes, including

chr19 and the distal end of chr7 (Figures 1E, 1F, and S1D). It was most striking that the deletion of chr19, the distal end of chr7, or both were observed in 70%, 78%, or 65% of the 23 GEM gliomas analyzed, respectively, thus recapitulating one of the most prevalent chromosomal abnormalities in human *IDH*-WT GBMs (Figures 1D–1F, S1D, and S1E). We further used qPCR analysis on an independent cohort of 11 *p53*$^{\Delta5-6}$-mutant-driven malignant gliomas, of which 82%, 73%, and 55% exhibited the loss of chr19, the distal end of chr7, and both, respectively (Figure 1G). These results demonstrate that the majority of *p53*$^{\Delta5-6}$-mutant-driven malignant gliomas, regardless of the absence or presence of the *Nf1* mutation, exhibit concurrent loss of chr19 and the distal end of chr7, both of which are syntenic to human 10q.

When a conditional heterozygous *Pten* mutation with a floxed exon 5 (*Pten*$^{+/E5}$) was introduced to the *p53*$^{\Delta5-6/\Delta5-6}$ model, the resultant *p53*$^{\Delta5-6/\Delta5-6}$;*Pten*$^{+/\Delta}$ mutant-driven gliomas exhibited Cre-mediated deletion of exon 5 but not unfloxed exon 9 (Figure 1H) (Zheng et al., 2008). In contrast, the *p53*-mutant-driven gliomas exhibited a reduction in both exons 5 and 9 of the *Pten* gene as a result of chr19 loss, which was predicted by both GISTIC and raw CNA data (Figure 1H). Similarly, high-grade malignant gliomas induced by conditional inactivation of *p53* and *Pten* (with or without *Rb*) also did not exhibit the chr19 loss reported in a previous study (Figure S1F) (Chow et al., 2011). These results demonstrate that targeted deletion of *Pten* abrogates chr19 loss, thus circumventing the selection of malignant glioma cells with a hallmark of chromosomal abnormalities (chr10q loss) in human primary GBMs.

Rictor/mTORC2 Deletion Delays *p53*-Mutant-Driven Malignant Glioma Formation

Given the frequent loss of chr19/*Pten* and the activation of the PI3K/Akt signaling pathway in these GEM malignant gliomas, we analyzed the effects of the conditional loss of one or two alleles of *Rictor* in the *p53*$^{\Delta5-6}$-mutant brain tumor model (hereafter referred to as *p53*$^{\Delta5-6/\Delta5-6}$*Rictor*$^{+/\Delta}$ or *p53*$^{\Delta5-6/\Delta5-6}$*Rictor*$^{\Delta/\Delta}$, compared to *p53*$^{\Delta5-6/\Delta5-6}$ mice) (Figure S3C). The loss of both alleles, not one allele of *Rictor*, significantly prolonged the lifespan of *p53*$^{\Delta5-6/\Delta5-6}$ mice with brain tumors (Figure 2A). Prolonged lifespan (>50%) and long-term survivors (>12 months) were predominately observed in *p53*$^{\Delta5-6/\Delta5-6}$*Rictor*$^{\Delta/\Delta}$ mice, which mainly resulted from a delay in the formation of malignant gliomas and tumors outside the brain (Figures 2B, S2A, and S2B). The majority of brain tumors were characterized as high-grade malignant astrocytic gliomas, including GBMs with expression of GFAP and Olig2, as well as high levels of p53$^{\Delta5-6}$-mutant protein (Figures 2C and S2C) (Louis et al., 2016). These results demonstrate that *Rictor* deletion extends survival by delaying *p53*$^{\Delta5-6}$-mutant-driven malignant glioma formation.

We have previously provided evidence that all malignant gliomas specifically accumulate high levels of mutant p53$^{\Delta5-6}$ protein, which appear to arise from p53$^{\Delta5-6+}$ glioma precursor cells that emerge from the subventricular zone (SVZ) stem cell niche at ~4–7 months of age (Ihrie and Alvarez-Buylla, 2011; Wang et al., 2009). Highly proliferating cell clusters expressing high levels of p53$^{\Delta5-6}$ protein were consistently identified in the corpus callosum, the rostral migratory stream, and the olfactory bulb—the areas associated with the SVZ stem cell niche, in 5 of 9 *p53*$^{\Delta5-6/\Delta5-6}$ brains analyzed at 6–7 months of age (Figures

2D–2F). In contrast, only 1 of 9 age-matched $p53^{5-6/5-6}Rictor^{-/-}$ brains had a similar p53$^{5-6}$/bromodeoxyuridine-positive (BrdU$^+$) cluster, which exhibited a significantly lower proliferation rate than those in the clusters of $p53^{5-6/5-6}$ brains (Figures 2F and 2G). Furthermore, p53^{5-6+} glioma precursor cells were largely restricted within the SVZ of this $p53^{5-6/5-6}Rictor^{-/-}$ brain, whereas glioma precursors were widely distributed in surrounding areas of the SVZ of $p53^{5-6/5-6}$ brains (Figures 2D, 2E, and S2D). Loss of both *Rictor* alleles also significantly reduced the proliferation rate in malignant gliomas analyzed at end stages (Figures 2H and 2I). These results demonstrate that Rictor/mTORC2 loss inhibits both tumor initiation and progression, thereby prolonging the survival of $p53^{5-6/5-6}Rictor^{-/-}$ mice with malignant gliomas.

We confirmed that all malignant gliomas only expressed the recombined $p53^{5-6}$ alleles, and both floxed *Rictor* alleles were recombined in the $p53^{5-6/5-6}Rictor^{-/-}$ gliomas (Figure S2E). Consistent with human GBMs, almost all *Rictor*-proficient gliomas in $p53^{5-6/5-6}$ and $p53^{5-6/5-6}Rictor^{+/-}$ mice exhibited robust expression of phosphorylated pAkt^{S473} and pAkt^{T308}, accompanied by the loss of Pten expression (Figures 2J and S2F). In contrast, *Rictor*-deficient gliomas in $p53^{5-6/5-6}Rictor^{-/-}$ mice showed little or no pAkt^{S473} and pAkt^{T308} expression without altering the total level of Akt (Figure 2J). The phosphorylation of Ndrg1 by another mTORC2 substrate, SGK1, was also significantly reduced in Rictor-deficient gliomas compared to *Rictor*-proficient gliomas (Figure 2J). These results demonstrate that *Rictor* deletion almost completely abolishes the mTORC2 activity for the phosphorylation of Akt^{S473} and Ndrg1^{T346}/SGK1, as well as Akt^{T308}, a PDK1 phosphorylation site that is strongly correlated with Akt kinase activity (Janku et al., 2018; Laplante and Sabatini, 2012). Although Rictor is not a subunit of mTORC1, decreased mTORC1 activity was observed in most *Rictor*-deficient malignant gliomas, as indicated by reduced phosphorylation of its direct substrates S6K^{T389} and 4E-BP1$^{T37/46}$ (Figure 2J). The effect of *Rictor* deletion on mTORC1 is likely an indirect consequence mediated by Akt inhibition, because Akt is known to activate mTORC1 by the phosphorylation of Tsc2 at T1462, which was significantly reduced in *Rictor*-deficient gliomas (Figure 2J) (Laplante and Sabatini, 2012). Together, these results demonstrate that *Rictor* deletion nearly completely inhibits mTORC2 and Akt activity and greatly reduces mTORC1 activity in $p53^{5-6}$mutant-driven malignant gliomas. Of note, the activation of other oncogenic pathways, including c-Myc, Erk/MAPK, and GSKβ-mediated signaling pathways, was not significantly different between Rictor-deficient and -proficient gliomas (Figures 2J and S2F). These observations demonstrate that despite a potent inhibition of three signaling pathways —mTORC2, Akt, and mTORC1 — *Rictor* deletion is not sufficient to completely eliminate $p53^{5-6}$- mutant-driven malignant glioma formation.

Rictor Deletion Promotes *p53*-Mutant-Driven Medulloblastoma Formation

Despite a robust inhibition of malignant gliomas and prolonged survival by *Rictor* deletion, a subset of the $p53^{5-6/5-6}Rictor^{-/-}$ mice developed malignant brain tumors at a rate that matched the $p53^{5-6/5-6}$ mice with the shortest tumor latency (Figure 2A). Almost all of the $p53^{5-6/5-6}Rictor^{-/-}$ mice in this subset developed MBs in the hindbrain, particularly in the cerebellum (Figure 3A). All of the $p53^{5-6}$-mutant-driven MBs, including $p53^{5-6/5-6}Rictor^{-/-}$ MBs, were characterized as large cell/anaplastic or classic pathology

with high cellular density, nuclear molding and Rosette structures, robust p53 $^{5-6}$ expression, and occasional neuronal (synaptophysin) and glial (GFAP) differentiation as seen in human MBs (Figure 3B) (Louis et al., 2016). These $p53$ $^{5-6}$-mutant-driven MBs exhibited robust Pax6 (a granule cell lineage-specific marker in the cerebellum) expression with minimal levels of Olig2. Conversely, $p53$ $^{5-6}$-mutant-driven malignant gliomas expressed high levels of Olig2 with minimal expression of Pax6 (Figures 3C–3E). This opposite expression pattern of Pax6 and Olig2 reliably distinguished MBs from malignant gliomas, even when both types of malignant brain tumors were observed in the cerebellum (Figure 3C) or in the different regions of the same brain (Figure 3D). In contrast to $p53$ $^{5-6}$-mutant-driven malignant gliomas, the majority of $p53$ $^{5-6}$-mutant-driven MBs, regardless of $Rictor$ status, exhibited low activities of mTORC2, Akt, and mTORC1 (Figures 3E and S3A). Furthermore, $Ptch1$-mutant-driven MBs, a well-established model for SHH-MBs, also exhibited low activities of these three signaling pathways even in the presence of WT $Rictor$ (Figures 3E and S3A) (Frappart et al., 2009). More important, $p53$ $^{5-6}$-mutant-driven MBs, not malignant gliomas, expressed high levels of Pax6, Gli1, and Atoh1, similar to $Ptch1$ mutant-driven SHH-MBs (Figures 3E and 3F). These results demonstrate that $p53$ $^{5-6}$-mutant MBs exhibit the critical molecular characteristics of pediatric SHH-MBs, including low activities of mTORC2/Akt and mTORC1 signaling pathways (Kool et al., 2014).

We found that $p53$ $^{5-6}$-mutant-driven MBs consistently developed more rapidly than malignant gliomas, arguing against the possibility that the increased MB incidence by $Rictor$ deletion results from extended lifespan as a consequence of inhibiting malignant gliomas (Figure S3B). Moreover, loss of one or two alleles of $Rictor$ on the $p53$ $^{5-6/}$ $^{5-6}Pten^{+/}$ -double mutant background also increased the MB incidence from 17% to 48% and 79%, respectively (Figures S3D-S3G). These observations demonstrate that $Rictor$ deletion, not potential differences in malignant glioma formation or genetic background, leads to a dramatic increase in SHH-MB incidence in both $p53$ $^{5-6/}$ $^{5-6}$ and $p53$ $^{5-6/}$ $^{5-6}Pten^{+/}$ mice.

Inhibition of Rictor/mTORC2-Dependent Akt Signaling Promotes SHH-MB Formation via Prolonging GCP Proliferation

We compared the gene expression profiles of the $p53$ $^{5-6}$-mutant-driven MBs with those of normal cerebellum; purified granule cell precursors (GCPs, the cells-of-origin of SHH-MBs); and mouse MBs with characteristics of SHH, WNT, and group 3 subgroups (Northcott et al., 2012). Our results showed that the gene expression profile of $p53$ $^{5-6}$-mutant-driven MBs was strongly associated with SHH-MBs and similar to GCPs, but not the group 3 and WNT MBs or normal cerebellar tissues (Figures 4A and 4B). Furthermore, all 22 $p53$ $^{5-6}$-mutant-driven MBs, irrespective of $Rictor$ genotype status, expressed high levels of Shh-specific genes, including $Gli1, Atoh1, Boc$, and $Sfrp1$, which were not expressed in $p53$ $^{5-6}$-mutant-driven malignant gliomas, the group 3 and WNT MBs, or normal cerebellar tissues (Figures S4A–S4C). qPCR analysis further confirmed that the Shh targets, including $Gli1, Gli2, N-Myc$, and $Atoh1$, were highly expressed in $p53$ $^{5-6}$-mutant-driven MBs at comparable levels to the $Ptch1$ mutant-driven SHH-MBs (Figure 4C). These results demonstrate that Rictor/mTORC2 loss significantly increases the incidence of SHH-MBs on the $p53$ $^{5-6}$-mutant background.

Rictor/mTORC2 loss does not significantly alter the latency or type of MBs on the *p53* [5–6]-mutant background (Figure 3A). Thus, we hypothesize that the increased incidence of SHH-MBs in *p53* [5–6/] [5–6]*Rictor* [/] mice results from the growth-promoting effects of GCPs, which constitute the external granular layer (EGL), a structure only transiently present in the developing cerebellum (Northcott et al., 2012). At postnatal day 16 (P16), both Pax6^{+} and proliferating Pax6^{+}BrdU[+] GCPs were readily identified in each folium of *Rictor*-deficient cerebella (regardless of *p53* mutational status), whereas almost no GCPs were present in most folia of control cerebella, accompanied by the disappearance of the EGL (Figures 4D–4F). Overall, the EGL of *Rictor*-deficient cerebella exhibited a 3-fold and 2-fold of increase in the cellular density and total number of proliferating GCPs, respectively (Figures 4G, S4D, and S4E).

To determine the cellular mechanism by which *Rictor* deletion promotes sustained proliferation of GCPs, we performed a BrdU pulse-chase assay to investigate cell-cycle exit of GCPs in *Rictor*-deficient versus *Rictor*-proficient cerebella from P15 to P17. Consistent with the observations at P16, only a small number of BrdU^{+} cells labeled at P15 were still detected at P17 in most of the control folia, most of which exited the cell cycle and migrated out of the EGL into the molecular layer (ML) or the internal granular layer (IGL) (Figures 4H and 4I). In contrast, the number of P15-labeled BrdU^{+} cells was dramatically increased in P17 *Rictor*-deficient cerebella, which was mainly caused by the cells sustained in the EGL, including proliferating BrdU[+]Ki67^{+} GCPs (Figures 4H, 4I, and S4F). When cerebellar development was complete at P22, *Rictor*-deficient cerebella exhibited ectopic accumulation of Pax6^{+} cells in the "persistent" EGL (Figures S4G–S4J). More important, abnormally proliferating Pax6^{+} GCPs were observed only in *Rictor*-deficient cerebella, particularly in folium 10b (Figures S4K and S4L). Together, these results are most consistent with a model wherein *Rictor* deletion delays timely differentiation of a subset of GCPs, prolonging their proliferation in the EGL.

Pharmacological Inhibition of Akt Signaling Delays GCP Differentiation via Stabilizing Atoh1 Protein

We investigated the molecular mechanism by which Rictor/mTORC2 loss leads to the delay in timely differentiation of GCPs during cerebellar development. First, we determined Rictor/mTORC2 activity during GCP development using the expression of pAkt[S473]. At the peak of migration of differentiating GCPs in P8 cerebella, almost no pAkt[S473] activity was observed in the EGL, while robust pAkt[S473] expression was found in the ML, and many differentiated neurons were found in the IGL (Figure 5A). Despite high levels of pAkt[S473] expressed in cell bodies and fibers of GFAP[+] Bergmann glial cells, a subset of migrating GCPs with high pAkt[S473] expression was identified in the ML (Figures 5A and S5A). When pAkt[S473] expression became restricted to cell bodies of Bergmann glial cells at P11, a subset of migrating GCPs with high levels of pAkt[S473] was readily identified in the ML (Figure 5B). More important, differentiated granule neurons in the IGL were the only cells with detectable pAkt[S473] expression in the adult cerebellum (Figure S5B). These results demonstrate that high levels of mTORC2/Akt activity are associated with differentiated cells in the granule cell lineage, including a subset of migrating and differentiating GCPs in the ML, and granule neurons in the IGL, but not in undifferentiated GCPs in the EGL.

Second, we sought to determine whether mTORC2-dependent Akt signaling is required for GCP differentiation. We therefore treated WT mice from P8 to P16 with BKM120, one of the most extensively tested pan-PI3K/AKT inhibitors in clinical trials (Janku et al., 2018). BKM120 treatment led to a reduction in the weight of the brain, mimicking the postnatal phenotypes observed in *Rictor*-deficient mice (Figures S5C–S5E and S5F–S5H). BKM120 treatment caused an increased number of proliferating GCPs in the EGL of multiple folia, thus recapitulating abnormally sustained proliferation of *Rictor*-deficient GCPs (Figures 5C–5E, S5I, and S5J). Similar to *Rictor*-deficient cerebella, an abnormal accumulation of GCPs was observed in the EGL of multiple folia of the BKM120-treated cerebella (arrowheads in Figures 5F, S5K, and S5L). BKM120 treatment increased the number of GCPs with expression of Atoh1, a transcription factor that is exclusively expressed in proliferating GCPs in the outer EGL (Figures 5G and 5H). Given that Atoh1 is required for maintaining an undifferentiated state of proliferating GCPs (Ayrault et al., 2010), these results raise the possibility that genetic and pharmacological inhibition of Akt signaling leads to increased Atoh1 expression, delaying timely differentiation of GCPs and prolonging their proliferation.

Third, we established and screened early-passage *p53* [5–6]-mutant-driven MB cell lines that maintained high levels of Atoh1 expression of their primary tumors, allowing us to investigate the regulation of endogenous Atoh1 protein (Figures 3E and 3F). In contrast to DMSO-treated cells, BKM120 treatment inhibited Akt activation and promoted accumulation of Atoh1 protein in a dose-dependent manner. At a low dose of 0.1 μM, BKM120 greatly inhibited Akt activation without inducing apoptosis (Figure 5I). Of note, a higher concentration at 0.5 μM, despite further inhibiting Akt activity, induced apoptosis at later time points. More important, BKM120-mediated accumulation of Atoh1 protein was observed in a time-dependent manner (Figure 5J). During the 24-hr treatment period, no significant difference in the number of cells or transcription of *Atoh1* mRNAs was observed (Figures S5M and S5N). Therefore, it is unlikely that BKM120 promotes the accumulation of Atoh1 protein via increasing cell numbers or *Atoh1* transcription. Instead, MG132, a proteasome inhibitor, also promoted the accumulation of Atoh1 protein in a time-dependent manner similar to BKM120, raising the possibility that Akt inhibition stabilizes Atoh1 protein by blocking ubiquitin-proteasome-mediated protein degradation (Figure 5K). We therefore measured the half-life of Atoh1 protein in MB cells treated with BKM120 or MLN4924 for 4, 8, 12, 16, and 24 hr in the presence of cycloheximide (CHX), which blocks new protein synthesis. MLN4924, a neddylation inhibitor of Cullin-RING E3 ubiquitin ligases (CRLs), blocks protein degradation by inhibiting neddylation of the Cullin protein of CRLs (Soucy et al., 2009). Both BKM120 and MLN4924 treatment significantly prolonged the half-life of Atoh1 protein from 4.56 hr in the DMSO-treated group, to 12.82 hr in the BKM120-treated group, and to 21.26 hr in the MLN4924-treated group (Figures 5L and 5M). BKM120-mediated Akt inhibition increases the half-life of Atoh1 protein, demonstrating that Akt signaling negatively regulates the protein stability of Atoh1, possibly by promoting CRL-mediated ubiquitylation and degradation. These results provide a molecular mechanism by which the inhibition of the mTORC2/Akt signaling pathway delays timely differentiation of GCPs and prolongs their proliferation.

p53-Mutant-Driven SHH-MBs Share Critical Features of *TP53* Mutant SHH-MBs in Humans

The persistent proliferation of *Rictor*-deficient GCPs exclusively observed on the $p53^{\Delta5-6/\Delta5-6}$ background suggests a p53-dependent cellular response or responses that drive the cell-cycle exit of abnormally proliferating *Rictor*-deficient Pax6$^+$ GCPs at the late stages of cerebellar development (Figures S6A–S6C). This tumor-suppressive response explains that Rictor/mTORC2 loss did not induce SHH-MBs on the $p53^{+/+}$ or $p53^{+/\Delta5-6}$ background. The activation of p53-mediated responses in *Rictor*-deficient GCPs was consistent with the observation that p53$^{\Delta5-6+}$ cells were readily identified in multiple folia of the $p53^{\Delta5-6/\Delta5-6}$Rictor$^{\Delta/\Delta}$, but not $p53^{\Delta5-6/\Delta5-6}$ cerebella at P22 (Figures 6A and 6B). Many $p53^{\Delta5-6/\Delta5-6}Rictor^{\Delta/\Delta}$ cerebella (4/7) but not $p53^{\Delta5-6/\Delta5-6}$ cerebella (n = 6) contained clusters of p53$^{\Delta5-6+}$ cells at P60, some of which were proliferating, reminiscent of MB precursor cells (Figures 6C and S6D). It is important to note that the percentage of proliferating cells expressing p53$^{\Delta5-6}$ (BrdU$^+$p53$^+$/BrdU$^+$) almost reached 80%–100% at P60 compared to 10%–20% in GCPs at P16, suggesting clonal selection from p53$^{\Delta5-6+}$ GCPs during postnatal development to MB precursor cells in young adult cerebella (Figures 6C and S6A–S6C). Thus, Rictor/mTORC2 loss expands and prolongs the GCP population that is susceptible to $p53^{\Delta5-6}$-mutant-driven SHH-MB formation during postnatal cerebellar development.

Although virtually all *p53*-deficient SHH-MBs of previously published mouse models harbor biallelic inactivation of *Ptch1* (Frappart et al., 2009), *TP53* mutant SHH-MBs in humans infrequently carry *PTCH1* mutations and have at least one normal *PTCH1* allele (Kool et al., 2014; Northcott et al., 2012). We performed qPCR, targeted deep sequencing of the *Ptch1* gene (~300×), and low-coverage whole-genome sequencing (~10×), demonstrating that a significant number of $p53^{\Delta5-6}$-mutant-driven SHH-MBs, regardless of *Rictor* status, retained at least one WT allele of *Ptch1* (Figure 6D, marked by *, and S6E). In particular, ~70% of *Rictor*-deficient SHH-MBs exhibited either WT or heterozygous *Ptch1*, with a high frequency of amplification of *N-Myc* and/or *Gli2*, the critical features of human *TP53* mutant SHH-MBs (Figures 6E, 6F, and S6F). In contrast, almost all *Ptch1* mutant-driven MBs analyzed in this study (>90%, n = 32) harbored biallelic *Ptch1* inactivation (via loss of *Ptch1* WT allele) (Figures 6D and S6E). Moreover, $p53^{\Delta5-6}$-mutant-driven SHH-MBs also exhibited other critical genomic features of human *TP53* mutant SHH-MBs, including heterozygous loss of chr10q/*PTEN* and chromosomal abnormalities such as tetraploidy, harboring four times the haploid number of chromosomes (Figures S6G–S6M, S7A, and S7B) (Kool et al., 2014). These results demonstrate that *Rictor* deletion promotes $p53^{\Delta5-6}$-mutant-driven SHH-MBs, which recapitulate the critical histopathological, molecular, genetic, and genomic features of *TP53* mutant SHH-MBs in humans. In summary, these observations demonstrate that *Rictor* deletion promotes the rapid generation of p53$^{\Delta5-6+}$ MB precursor cells from GCPs in the EGL during late stages of cerebellar development, while delaying the emergence of p53$^{\Delta5-6+}$ glioma precursor cells from the SVZ stem cell niche of the adult brain (Figure S7C).

Impact of *RICTOR* Expression in Pediatric SHH-MBs and Adult GBMs in Humans

Despite high levels of similarity between mouse $p53^{\Delta5-6}$-mutant SHH-MBs and human *TP53* mutant SHH-MBs, no homozygous deletion of *RICTOR* was identified in human

SHH-MBs (Kool et al., 2014). We therefore used a bioinformatics approach to divide pediatric SHH-MBs into "*RICTOR*-high" and *"RICTOR*-low" groups based on mRNA expression data (see STAR Methods). The SHH-MBs within the *RICTOR*-low group were associated with poor survival among pediatric SHH-MBs (Figures 7A and 7B). *TP53* mutant SHH-MBs are one of the two MB subgroups with the worst survival rates and are responsible for the majority of the mortality associated with SHH-MBs (Kool et al., 2014; Northcott et al., 2012). The majority of *TP53* mutant SHH-MBs (~65%) were consistently observed in the group, with the lowest *RICTOR* expression found among SHH-MBs (Figures 7A and7B). Thus, the poor survival of the *RICTOR*-low group is at least partially contributed to by an enrichment of *TP53* mutant SHH-MBs. Among *TP53-WT* SHH-MBs, more pediatric patients with lower levels of *RICTOR* expression died during the follow-up studies (Figures 7C and 7D). These results suggest that low levels of *RICTOR* expression may negatively affect patient survival independent of its association with *TP53* mutations, although a large number of patients with SHH-MBs are needed to validate this observation.

Given that the mTORC2-dependent AKT signaling is the major downstream effect of the PI3K/PTEN pathway, we further determined the frequency of mutational events in the PI3K/AKT pathway in SHH-MBs and compared them to adult primary GBMs, most of which exhibit genetic alterations in the PI3K/AKT pathway (Brennan et al., 2013). Approximately 32% of infant, 39% of childhood, and 16% of adult SHH-MBs exhibited the loss of one copy of chr10q/*PTEN* (heterozygous loss) (Figures 7E and 7F). In contrast, nearly all *IDH*-WT GBMs (97% of 221 cases in The Cancer Genome Atlas [TCGA] database) exhibited chr10q/*PTEN* loss (Figure 7F) (Brennan et al., 2013). More important, biallelic inactivation of *PTEN* caused by homozygous deletions or additional loss-of-function mutations in the second alleles was observed in 41% of adult primary GBMs, which rarely occurred in infant (6%) and adult SHH-MBs (4%) and none in childhood SHH-MBs (0%), the age group that harbors the most *TP53* mutations (Figures 7F and 7G). Genetic alterations in the *PIK3CA* were also rare in pediatric SHH-MBs (infant, 6% and childhood, 0%) (Figure 7E). Together, high versus low frequency of genomic and molecular alterations in the PI3K/AKT signaling pathway in human adult primary GBMs versus pediatric SHH-MBs are consistent with the opposing tumor-promoting versus tumor-suppressing effects of Rictor/mTORC2-dependent Akt signaling observed in our mouse studies. In support, adult *IDH*-WT/non-G-CIMP GBMs with high levels of *RICTOR* mRNA expression were associated with poor survival, particularly for the patients surviving >7 months (Figures 7H–7J). RICTOR is the only component of mTORC2 or mTORC1 whose mRNA expression level has an opposite relation to survival of pediatric SHH-MBs and adult GBMs (Figure S8).

DISCUSSION

The unique aspect of the conditional *p53* [5–6] brain tumor model is that the driving *p53* [5–6] mutation itself does not directly provide growth advantage but instead allows spontaneous accumulation of oncogenic alterations in targeted cells, which in turn drive malignant transformation. Despite the *p53* [5–6] mutation being conditionally targeted toward embryonic neural stem cells and mature astrocytes, no tumor in the brain was observed until late adulthood (6–12 months) (Figure 3A) (Wang et al., 2009, 2012). The cell- or cells-of-origin

of these $p53$ [5–6]-mutant-driven brain tumors must be the cells with self-renewing potentials (e.g., neural stem and progenitor cells) that can undergo multiple cell divisions, allowing spontaneous accumulation of oncogenic alterations sufficient for malignant transformation (Ihrie and Alvarez-Buylla, 2011; Northcott et al., 2012). Thus, the conditional $p53$ [5–6] brain tumor model provides an experimental system with which to discover and validate oncogenic drivers that accumulate in neural stem and progenitor cell populations, which would directly confer growth advantage during the initiation and progression of $p53$ [5–6]-mutant-driven malignant gliomas and SHH-MBs.

The vast majority of $p53$ [5–6]-mutant mice acquire chr19/*Pten* loss during malignant glioma formation. The presence of additional *Pten*$^{+/-}$ mutation on the $p53$ [5–6]-mutant background circumvents chr19/*Pten* loss, which is also absent in GFAP-creER (estrogen receptor)-driven *p53/Pten*-double or *p53/Pten/Rb*-triple mutant models (Chow et al., 2011). These observations suggest that the major target of chr19 loss is the *Pten* tumor-suppressor gene, which consequently activates the PI3K/Akt signaling pathway in this glioma model. Rictor/mTORC2 loss consistently inhibits Akt signaling, thereby reducing the incidence and delaying the formation of malignant gliomas and GBMs in both $p53$ [5–6]-mutant and $p53$ [5–6]/*Pten*$^{+/-}$-double mutant-driven models. Recent studies using human GBM cells have demonstrated that RICTOR/mTORC2 integrates intracellular growth factor receptor signaling with extracellular nutrient availability, reprogramming cancer metabolism and causing drug resistance of PI3K/AKT/mTOR inhibitors (Masui et al., 2013, 2015; Wu et al., 2014). The availability of GEM *Rictor*-proficient and *Rictor*-deficient malignant gliomas and GBMs provides an *in vivo* experimental system with an immunocompetent environment in which to investigate Akt-dependent and Akt-independent mechanisms of mTORC2 in reprogramming GBM metabolism. Furthermore, preclinical studies will be performed to target metabolic vulnerability caused by mTORC2 inhibition in these GEM models. Despite the potent inhibition of mTORC1, mTORC2, and Akt signaling pathways, it should be noted that the emergence of *Rictor*-deficient gliomas highlights the utility of this glioma model to investigate therapeutic resistance to PI3K/AKT/mTOR inhibitors.

We have identified a novel tumor-suppressive function of Rictor/mTORC2 in the pathogenesis of $p53$ [5–6]-mutant-driven SHH-MBs. It has been well documented that neural stem cells in the SVZ stem cell niche remain undifferentiated throughout the lifespan, providing the opportunity for $p53$ [5–6]-mutant cells to accumulate oncogenic alterations that are sufficient for malignant glioma/GBM formation (Ihrie and Alvarez-Buylla, 2011; Wang et al., 2009; Zhu et al., 2005). However, GCPs are a transient precursor population during cerebellar development, which must accumulate oncogenic alterations during a limited developmental window to generate MB precursors (Northcott et al., 2012). Mechanistically, *Rictor* deletion causes a delay in timely differentiation of a subset of GCPs, whose differentiation is associated with the activation of mTORC2/Akt signaling. Consequently, these *Rictor*-deficient GCPs abnormally continue to proliferate in the persistent EGL. The sustained proliferating GCPs therefore increase the population size for tumor-susceptible cells to accumulate oncogenic alterations (e.g., *Gli2* and/or *N-Myc* amplification), leading to increased SHH-MB penetrance on the $p53$ [5–6]-mutant background. These observations suggest that the shift of the tumor spectrum from malignant gliomas to SHH-MBs results

from the opposing role of Rictor/mTORC2 in neural stem cells in the adult SVZ versus GCPs in the EGL in the postnatal developing cerebellum (Figure S7C).

Pharmacological inhibition of the PI3K/Akt signaling pathway during postnatal cerebellar development blocks GCP differentiation and increases the sustained proliferating GCP population during postnatal cerebellar development (Dimitrova and Arcaro, 2015). Thus, the effects of this PI3K/AKT inhibitor treatment partially mimic the delayed differentiation and sustained proliferation of GCPs observed in *Rictor*-deficient cerebella. Along with the observation that highly phosphorylated Akt^{Ser473} is associated with the differentiation of GCPs, these results demonstrate a critical role for Rictor/mTORC2-dependent Akt signaling in promoting differentiation of a subset of GCPs and suppressing SHH-MB formation. Increased numbers of GCPs with Atoh1 expression observed in BKM120-treated cerebella suggest a mechanistic basis of the negative role of Rictor/mTORC2/Akt signaling in GCP proliferation. We provide direct evidence that Akt inhibition promotes the accumulation of Atoh1 protein, possibly via blocking CRL-mediated protein degradation. These results provide a molecular mechanism for a recent clinical observation that no or low levels of AKT or mTORC1 activity are detected in most pediatric SHH-MBs (Kool et al., 2014). We also observed low AKT activation in 5 human MB-derived cell lines (3 SHH-MB lines and 2 group 3/4 lines), which are more resistant to a PI3K/AKT inhibitor compared to GBM cell lines (S.A., unpublished data). It will be important to validate the tumor-suppressive functions of mTORC2/AKT signaling in patient-derived cell lines and xenograft models of MBs. Thus, our study suggests that caution should be taken in the design of clinical trials using PI3K/AKT/mTOR inhibitors to treat brain tumors in children (Dimitrova and Arcaro, 2015; Janku et al., 2018).

STAR★METHODS

CONTACT FOR REAGENT AND RESOURCE SHARING

Further information and requests for reagents should be directed to the Lead Contact Yuan Zhu (yzhu@childrensnational.org).

EXPERIMENTAL MODEL AND SUBJECT DETAILS

The mutant mice used in this study had various genotypic configurations: For brain tumor formation, hGFAP-cre;*p53*$^{flox/flox}$, hGFAP-cre;*p53*$^{flox/flox}$;*Rictor*$^{flox/+}$, and hGFAP-cre;*p53*$^{flox/flox}$;*Rictor*$^{flox/flox}$ mice were used. A second group of mice as a validation cohort carried additional heterozygous *Pten*$^{flox/+}$ mutation. Brain tumors from a group of *Ptch1*$^{+/-}$ mice with the genotype of hGFAP-cre;*Ptch1*$^{+/-}$ and hGFAP-cre;*p53*$^{flox/flox}$;*Ptch1*$^{+/-}$; were used as SHH-MB controls. For developmental biology studies, we utilized a non-tumorigenic mutant mouse model with the genotype of hGFAP-cre;*p53*$^{flox/+}$;*Rictor*$^{flox/flox}$. The control group was a collection of hGFAP-cre$^{(negative)}$ mice that were phenotypically indistinguishable and completely healthy. Age and littermate-matched control and mutant mice were used for the developmental analyses to minimize the impact of modifier genes. Brain tumor mice were either littermates or close relatives collected over approximately 9 years. All mice except for the original *Ptch1*$^{+/-}$ allele that contained the FVB background were maintained in the mixed backgrounds of C57Bl6 and 129S1/Svj. The phenotypes of

both malignant gliomas/GBMs and SHH-MBs were similarly observed in male and female mice. Consequently, similar numbers of mice with both genders were used for the experiments. Mice were cared for according to the guidelines that were approved by the Animal Care and Use Committees of the University of Michigan at Ann Arbor and Children's National Medical Center, Washington, DC.

METHODS DETAILS

Genotyping and PCR—Taq 2X MeanGreen Master Mix (Empirical Bioscience) was used in PCR experiments along with the following primer sets for tail and tumor tissue genotyping. See primer information in Table S2.

Tissue Preparation, Histopathology and Tumor Diagnosis—Approximately 65%–70% of the mice were sacrificed due to observable neurological symptoms including enlarged head, tremor, seizure, ataxia, or lack of balance indicating the presence of an end-stage brain tumor. One set of these mice were perfused using 4% paraformaldehyde (PFA), brains were collected and kept in 4% PFA for at least one day. The second set of mice were sacrificed using cervical dislocation procedure after anesthesia with 3.5% Tribromoethanol (Avertin). The brains were collected at 4°C, rinsed in 4°C PBS and cut sagittally along the midline. One half of the brain was kept in 4% PFA while the other half was used for frozen tissue collection, snap freezing in liquid nitrogen, and cell culture preparation. Processed and paraffin embedded brain samples were sectioned sagittally at 5 μm and collected on Superfrost Plus microscope slides (Fisher Scientific). Hematoxylin and eosin (H&E) staining was performed approximately every 10 slides and adjacent sections were subjected to immunohistochemical analysis using the antibodies for p53, Olig2, GFAP, Synaptophysin and Pax6. Samples were analyzed under a light microscope by two investigators (SCP and SA) based upon the World Health Organization (WHO) criteria of the classification of tumors in the CNS (Louis et al., 2016). Diagnosed high-grade malignant gliomas included anaplastic astrocytoma, glioblastoma, anaplastic oligoastrocytoma and anaplastic oligodendroglioma. Final diagnoses were reached as a consensus of H&E staining findings and immunohistochemical analyses. In rare cases where a clear diagnosis was hard to reach, Olig2 and Pax6 immunohistochemistry staining (described below) were taken as conclusive criteria as Olig2 is characteristic of high-grade malignant gliomas whereas Pax6 labels medulloblastomas.

Immunohistochemistry and Immunofluorescence—Adjacent paraffin sections were used in immunohistochemistry and immunofluorescence analyses. Slides were first deparaffinized through a series of Xylene, Ethanol and PBS treatments, boiled in Retrieve-All antigen unmasking system (Covance), permeabilized in 0.3% Triton X-100 (Sigma-Aldrich) and blocked with 5% normal goat serum or normal donkey serum prior to overnight primary antibody incubation at 4°C. The visualization of the primary antibodies in immunohistochemistry was performed with the avidin/biotin-based peroxidase system (Vectastain Elite ABC System, Vector Laboratories), except for pAkt[S473] and Pten, for which SignalStain Boost IHC Detection Reagent HRP-rabbit (Cell Signaling) was used. The dilutions of the primary antibodies used on paraffin sections in immunohistochemistry study were: p53 (1:500, rabbit, Leica), Olig2 (1:2,000, rabbit, Millipore), GFAP (1:1,000, rabbit,

Dako), Synaptophysin (1:200, rabbit, Covance), Pax6 (1:500, rabbit, Covance), Ki67 (1:500, rabbit, Abcam), pAkt^{S473} (1:200, rabbit, Cell Signaling), Pten (1:400, rabbit, Cell Signaling) and Atoh1 (1:500, rabbit, gift from Dr. Jane Johnson from UT Southwestern). Hematoxylin was used as a counterstain to label cell nuclei. Sections were examined under a light microscope (Olympus BX51 and BX53).

For Atoh1 IHC on paraffin sections, we tested three different Atoh1 antibodies: two mouse antibodies from Abcam (Ab27667) and DSHB (Atoh1 concentrate) and one rabbit antibody (gift from Dr. Jane Johnson from UT Southwestern). Only the rabbit Atoh1 antibody gives the strongest and robust staining on SHH-MBs paraffin sections with small modifications of the IHC protocol mentioned above. For the DAB reaction step, we put the tissue slides on ice to slow down the reaction and reduce some background staining. The freshness of tissue samples has big impact on the Atoh1 staining, with high staining in more fresh samples. We performed Atoh1 IHC on total 46 SHH-MBs including $p53^{5-6/\ 5-6}Ptch^{+/-}$ (n = 4); $p53^{5-6/\ 5-6}$ (n = 3), $p53^{5-6/\ 5-6}Rictor^{+/}$ (n = 17) and $p53^{5-6/\ 5-6}Rictor^{/}$ (n = 22). Over 80% of the tumor samples have extensively high level of Atoh1 expression, a signature of SHH MBs.

The visualization of the primary antibodies in immunofluorescence was performed with the use of the Alexa488, Alexa555 and Alexa647 conjugated secondary antibodies (1:400, Invitrogen, Life Technologies). Primary antibodies used for immunofluorescence were: p53 (1:500, rabbit, Leica), BrdU (1:500, rat, Abcam), Olig2 (1:2,000, rabbit, Millipore), Ki67 (1:500, rabbit, Abcam), Ascl1 (1:100-1:200, mouse, BD PharMingen), GFAP (1:1,000-1:2,000, rabbit, Dako), Nestin (1:100, mouse, Millipore), Sox2 (1:250, goat, Santa Cruz Biotech), Pax6 (1:500, rabbit, Covance), Calbindin (1:1000, mouse, Sigma) and NeuN (1:500, mouse, Millipore). For pAkt^{S473} (1:300, rabbit, Cell Signaling) staining, biotin-conjugated secondary antibody was used, followed by signal amplification with Alexa555-conjugated streptavidin (Thermo Fisher Scientific, S-32355). DAPI was used as a counterstain to label individual cell nuclei. Sections were examined under a fluorescent microscope (Olympus BX53).

BrdU Assay for the Analyses of Proliferation and Differentiation—For the proliferation assay, mice were injected with 50 μg of BrdU per gram of body weight. Embryonic and newborn mice received one injection, pups and neonatal mice up to 30 days old received two, mice around two months old received three and adult mice older than two months old received five injections, with multiple injections applied at two hour-intervals. All of the mice were perfused with 4% PFA two hours after the final BrdU injection. For the differentiation assay, P15 mice were injected with a 50 μg of BrdU per gram of body weight pulse and perfused with 4% PFA following a 48-hour chase. In both assays, brains were dissected and processed for either paraffin-embedded or cryostat sections. BrdU immunofluorescence was performed as described previously (Wang et al., 2009).

BKM120 Treatment Study—The wild-type pups were injected with 10mg/KG BKM120 (Selleckchem, S2247) or Vehicle (10% Kolliphor EL (Sigma-Aldrich, C5135), 10% PEG400 (Sigma-Aldrich, 202398)) daily from P8 to P16. After the injection at P16, the mice were

injected with 50 μg of BrdU per gram of body weight for two times at two hour-intervals. Then the mice were collected as mentioned above.

Identification of p53 $^{5\text{-}6}$-positive Early Tumor Precursors for Malignant Glioma and Medulloblastoma—Early glioma precursors are defined as p53 $^{5\text{-}6}$-positive cell clusters (> 20 cells per high magnification view) in brain regions (e.g., corpus callosum) outside the SVZ/RMS germinal zone in 4-7 month old *p53* $^{5\text{-}6/}$ $^{5\text{-}6}$ brains. Early medulloblastoma precursors are defined as p53 $^{5\text{-}6}$-positive cell clusters (> 10 cells per high magnification view) in the "persistent" EGL in the cerebella of *p53* $^{5\text{-}6/}$ $^{5\text{-}6}$ (with or without *Rictor* deletion) at the age of P22 or older. At these time points, there is almost no proliferation in aforementioned brain regions in control mice. In *p53* $^{5\text{-}6/}$ $^{5\text{-}6}$ (with or without *Rictor* deletion) brains, although not all the p53 $^{5\text{-}6}$-positive cells in the cluster are BrdU$^+$, the majority of BrdU$^+$ abnormal proliferating cells are p53 $^{5\text{-}6}$-positive, which provides the basis of using the p53 $^{5\text{-}6}$ marker to label the early tumor precursor cells in the morphologically normal brains.

Western Blotting Analysis—Snap-frozen tissue samples from wild-type control brains and tumors were homogenized in Pierce RIPA Buffer (Thermo Fisher Scientific) (10 μL buffer/1 mg tissue), mixed 1:1 with Laemmli Sample Buffer (BioRad) and boiled at 100°C for 8 minutes. Samples were then subjected to SDS-PAGE using the Criterion TGX Precast gels (BioRad) and transferred onto PVDF membranes (Millipore). The membranes were blocked in 5% non-fat milk prepared in TBST and prior to an overnight incubation with primary antibodies at 4°C. Next the membranes were washed with TBST and incubated in horseradish peroxidase (HRP)-conjugated secondary antibodies at room temperature for 1 hour. Signal was detected using Pierce ECL Western Blotting Substrate (Thermo Fisher Scientific). The primary antibodies used in this study were as follows: pAkt^{S473} (1:1,000, rabbit, Cell Signaling), pAkt^{T308} (1:1,000, rabbit, Cell Signaling), Akt (1:1,000, rabbit, Cell Signaling), pNDRG1^{T346} (1:1,000, rabbit, Cell Signaling), Pten (1:1,000, rabbit, Cell Signaling), Rictor (1:500, rabbit, gift from Dr. D. Fingar at University of Michigan), mTOR (1:1,000, rabbit, Cell Signaling), β-Actin (1:5,000-10,000, mouse, Sigma-Aldrich), pS6K^{T389} (1:1,000, rabbit, Cell Signaling), p4E-BP1$^{T37/46}$ (1:1,000, rabbit, Cell Signaling), pTSC2^{T1462} (1:1,000, rabbit, Cell Signaling), pS6$^{S240/244}$ (1:2,000, rabbit, Cell Signaling), S6 (1:2,000, rabbit, Cell Signaling), Olig2 (1:4,000, rabbit, Millipore), cMyc (1:1,000, rabbit, Cell Signaling), pErk1/2$^{T202/Ty204}$ (1:1,000, rabbit, Cell Signaling), Erk1/2 (1:1,000, rabbit, Cell Signaling), pGSK-3β^{S9} (1:2,000, rabbit, Cell Signaling), P120 (1:1000, mouse, BD Biosciences), Pax6 (1:1,000, rabbit, Covance), Gli1 (1:500, rabbit, Cell Signaling) and Ezh2 (1:1,000-1:2,000, rabbit, Cell Signaling) and Atoh1 (1:1000, Rabbit, Abcam, ab168374). HRP-conjugated secondary antibodies were anti-mouse (1:5,000-1:10,000, goat, BioRad) and anti-rabbit (1:5,000-1:10,000, goat, BioRad).

Tumor-Sphere Cell Culture and Chromosome Assay—End-stage tumors were dissected at 4°C and tissue was then transferred into DMEM medium, followed by enzymatic cell dissociation using Accutase (Innovative Cell Technologies). Cell cultures were prepared in self-renewal medium based on an established protocol (Wang et al., 2012). Cell density was quantified using a hemocytometer, (Counting Chamber, Hausser Scientific)

and approximately 20,000-100,000 cells/well were plated into 6-well ultra-low attachment surface polystyrene plates (Corning) for primary tumor-sphere cultures. The medium was changed every 3-5 days and the cultured cells were passaged into two new 6-well plates after 1-2 weeks based on the growth rate and passage number. Chromosome analyses were conducted using primary cell lines based on a metaphase preparation protocol as previously described (Frappart et al., 2009). According to this protocol, cells were grown for 24 hours, treated with 100 ng/ml KaryoMax Colcemid solution (GIBCO, Life Technologies) for 1 hour to arrest proliferation at metaphase. Cells were then treated with 0.4% KCl at 37°C, fixed in ice cold Methanol:Glacial acetic acid (3:1) solution overnight and dropped on Superfrost Plus microscope slides (Fisher Scientific). Chromosomes of metaphase cells were stained with DAPI. Cell lines analyzed at passage 1 and 2 are considered "early passage" and those analyzed at subsequent passages are considered as "late passage."

RT-PCR for Copy Number Analyses—Total genomic DNAs were extracted from frozen wild-type control brain tissues, high-grade gliomas and medulloblastomas by using an AllPrep DNA/RNA Mini Kit (QIAGEN). Depending on the sample concentration, various amounts of template DNA (average 100 ng/reaction) along with the SYBR Select Master Mix (Thermo Fisher Scientific) and primers were used in RT-PCR. See primer information in Table S2.

CT value ($CT_{testGene}$ - $CT_{reference}$) and then [$1/CT^2$] is calculated for each sample. The average of the readings from the wild-type control tissue were set to "1" and all of the samples were calculated accordingly. *β-Actin* (chr5) and *Gapdh* (chr7), and *Tfrc* (chr16) were used as reference genes (internal controls). We additionally used TaqMan Copy Number Assays along with the compatible CopyCaller Software. *Tfrc* (chr16) was used as a reference gene in this set of analyses. The primer sets were as follows:

N-Myc

Mycn_Mm00378993_cn

Gli2

Gli2_Mm00026939_cn

Tfrc

TaqMan Copy Number Reference Assay, mouse, Tfrc

The estimated copy numbers based on *β-Actin, Gapdh*, and *Tfrc* were compared to each other to confirm the accuracy and the consistency of the copy number calculations. Then, the average of the three readings were shown in the figures.

RT-PCR for Gene Expression Analyses—cDNA synthesis, using RNA collected as described, was performed using QuantiTect Reverse Transcription Kit (QIAGEN), along with approximately 300ng of RNA for each sample. RT-PCR experiments were carried out

in the 7500 Real-Time PCR System (Applied Biosystems) using SYBR Select Master Mix (Applied Biosystems) and primers. See primers information in Table S2.

CT value ($CT_{testGene}$ - CT_{Gapdh}) and then [$1/CT^2$] is calculated for each sample. The average of the readings from the *Ptch1+*[+/−] model medulloblastomas was set to "100" and all of the samples were calculated accordingly. Wild-type control brain tissue and gliomas were used as negative controls for medulloblastoma samples.

Protein half-life analysis of Atoh1—A *p53* [5-6/ 5–6] medulloblastoma cell line (CKO2 L2) was treated with 200 μg/ml cycloheximide (Sigma, C7698-1G) together with vehicle (DMSO), BKM120 and MLN4924 (Selleckchem, S7109) as indicated. Then the cells were collected at indicated time points for IB assay. The Atoh1 level was quantified by densitometry analysis using ImageJ (1.50i) image processing software. The ratio of Atoh1/β-Actin was calculated and statistical analysis was performed using Prism 7 with Two-way ANOVA analysis.

Bioinformatics—Affymetrix GeneChip Mouse Genome 430 2.0 Array was used for the gene expression profiles of the glioma and medulloblastoma samples. Unsupervised hierarchical cluster analyses were performed in categorization of the samples. Agilent 44K/100K cDNA and/or oligochip were used for the copy number analyses of the glioma samples. The genotypes of the MB samples used in these analyses are: *p53* [/] (n = 3), *p53* [5-6/ 5-6]*Rictor*[+/] (n = 2), *p53* [5-6/ 5-6]*Rictor* [/] (n = 5), *p53* [5-6/ 5-6]*Pten*[+/] (n = 3), *p53* [5-6/ 5-6]Pten[+/] *Rictor*[+/] (n = 6, three of which had germline *Rictor* mutation), and *p53* [5-6/ 5-6]*Pten*[+/] *Rictor* [/] (n = 3).

Low-coverage whole genome sequencing (lgWGS) was used to infer the copy number changes in mouse medulloblastomas. The read counts per 1kb along each gene's chromosomal region is plotted, and the copy number changes in tumor samples were calculated in comparison to matched tail DNA.

The Kaplan scanner tool in R2 was used to find the best cut-off in expression within a certain group of tumors for which the Kaplan Meier analysis gives the lowest log rank p value. This p value was corrected for multiple testing as multiple tests were performed to find the lowest p value. The plots that we showed in Figure 7 and Figure S8 were thus the plots with lowest p values. All other cut-offs gave higher p values. Of course, the cut-offs can then be different between each subgroup. However, as overall expression levels are also different between subgroups, it still makes sense to use different cut-offs. R2 is a microarray analysis and visualization platform that is freely available online: https://hgserver1.amc.nl/cgi-bin/r2/main.cgi.

Schematic representations of the mouse chr19 and chr7, and human chr10 were prepared based on the information in Ensembl database.

QUANTIFICATION AND STATISTICAL ANALYSIS

Kaplan-Meier survival curves were used to compare the survivorship of the mice sacrificed due to brain tumors, soft tissue sarcomas and/or other health concerns. The Mantel-Cox

(Log-rank) test was used to compare the curves statistically. Anatomically comparable sections from control and mutant brains were visualized at 20X and 40X magnifications. Multiple images were captured and subjected to double-blinded analysis to measure the specific areas (i.e., cerebellar surface area) and to quantify the number of the cells using ImageJ software. At least three animals were used from each group, and two-tailed Student's t test was used to compare the number and percentage of the different cellular populations. Fisher's exact test was used to compare the mouse models in terms of the tumor location and tumor spectrum. Linear regression analysis was performed in RT-PCR experiments for copy number estimates comparing the readings based on two different reference genes. The coefficient of determination (R^2) and p values were calculated. Data were presented as mean ± Standard Deviation (SD) or Standard Error of the Mean (SEM), and $p < 0.05$ was considered to be statistically significant in all of the statistical analyses.

DATA AND SOFTWARE AVAILABILITY

The accession number for the gene expression data reported in this paper is GEO: GSE78895.

Supplementary Material

Refer to Web version on PubMed Central for supplementary material.

ACKNOWLEDGMENTS

REFERENCES

Ayrault O, Zhao H, Zindy F, Qu C, Sherr CJ, and Roussel MF (2010). Atoh1 inhibits neuronal differentiation and collaborates with Gli1 to generate medulloblastoma-initiating cells. Cancer Res. 70, 5618–5627. [PubMed: 20516124]

Baysan M, Bozdag S, Cam MC, Kotliarova S, Ahn S, Walling J, Killian JK, Stevenson H, Meltzer P, and Fine HA (2012). G-cimp status prediction of glioblastoma samples using mRNA expression data. PLoS One 7, e47839. [PubMed: 23139755]

Brennan CW, Verhaak RG, McKenna A, Campos B, Noushmehr H, Salama SR, Zheng S, Chakravarty D, Sanborn JZ, Berman SH, et al.; TCGA Research Network (2013). The somatic genomic landscape of glioblastoma. Cell 155, 462–477. [PubMed: 24120142]

Chow LM, Endersby R, Zhu X, Rankin S, Qu C, Zhang J, Broniscer A, Ellison DW, and Baker SJ (2011). Cooperativity within and among Pten, p53, and Rb pathways induces high-grade astrocytoma in adult brain. Cancer Cell 19, 305–316. [PubMed: 21397855]

Dimitrova V, and Arcaro A (2015). Targeting the PI3K/AKT/mTOR signaling pathway in medulloblastoma. Curr. Mol. Med. 15, 82–93. [PubMed: 25601471]

Frappart PO, Lee Y, Russell HR, Chalhoub N, Wang YD, Orii KE, Zhao J, Kondo N, Baker SJ, and McKinnon PJ (2009). Recurrent genomic alterations characterize medulloblastoma arising from DNA double-strand break repair deficiency. Proc. Natl. Acad. Sci. USA 106, 1880–1885. [PubMed: 19164512]

Guertin DA, Stevens DM, Saitoh M, Kinkel S, Crosby K, Sheen JH, Mullholland DJ, Magnuson MA, Wu H, and Sabatini DM (2009). mTOR complex 2 is required for the development of prostate cancer induced by Pten loss in mice. Cancer Cell 15, 148–159. [PubMed: 19185849]

Ihrie RA, and Alvarez-Buylla A (2011). Lake-front property: a unique germinal niche by the lateral ventricles of the adult brain. Neuron 70, 674–686. [PubMed: 21609824]

Janku F., Yap TA, and Meric-Bernstam F (2018). Targeting the PI3K pathway in cancer: are we making headway? Nat. Rev. Clin. Oncol. 15, 273–291. [PubMed: 29508857]

Kalaitzidis D, Sykes SM, Wang Z, Punt N, Tang Y, Ragu C, Sinha AU, Lane SW, Souza AL, Clish CB, et al. (2012). mTOR complex 1 plays critical roles in hematopoiesis and Pten-loss-evoked leukemogenesis. Cell Stem Cell 11, 429–439. [PubMed: 22958934]

Kim H, Zheng S, Amini SS, Virk SM, Mikkelsen T, Brat DJ, Grimsby J, Sougnez C, Muller F, Hu J, et al. (2015). Whole-genome and multisector exome sequencing of primary and post-treatment glioblastoma reveals patterns of tumor evolution. Genome Res. 25, 316–327. [PubMed: 25650244]

Kool M, Jones DT, Jäger N, Northcott PA, Pugh TJ, Hovestadt V, Piro RM, Esparza LA, Markant SL, Remke M, et al.; ICGC PedBrain Tumor Project (2014). Genome sequencing of SHH medulloblastoma predicts genotype-related response to smoothened inhibition. Cancer Cell 25, 393–405. [PubMed: 24651015]

Laplante M, and Sabatini DM (2012). mTOR signaling in growth control and disease. Cell 149, 274–293. [PubMed: 22500797]

Louis DN, Perry A, Reifenberger G, von Deimling A, Figarella-Branger D, Cavenee WK, Ohgaki H, Wiestler OD, Kleihues P, and Ellison DW (2016). The 2016 World Health Organization Classification of Tumors of the Central Nervous System: a summary. Acta Neuropathol. 131, 803–820. [PubMed: 27157931]

Magee JA, Ikenoue T, Nakada D, Lee JY, Guan KL, and Morrison SJ (2012). Temporal changes in PTEN and mTORC2 regulation of hematopoietic stem cell self-renewal and leukemia suppression. Cell Stem Cell 11, 415–428. [PubMed: 22958933]

Masui K, Tanaka K, Akhavan D, Babic I, Gini B, Matsutani T, Iwanami A, Liu F, Villa GR, Gu Y, et al. (2013). mTOR complex 2 controls glycolytic metabolism in glioblastoma through FoxO acetylation and upregulation of c-Myc. Cell Metab. 18, 726–739. [PubMed: 24140020]

Masui K, Tanaka K, Ikegami S, Villa GR, Yang H, Yong WH, Cloughesy TF, Yamagata K, Arai N, Cavenee WK, and Mischel PS (2015). Glucose-dependent acetylation of Rictor promotes targeted cancer therapy resistance. Proc. Natl. Acad. Sci. USA 112, 9406–9411. [PubMed: 26170313]

Mermel CH, Schumacher SE, Hill B, Meyerson ML, Beroukhim R, and Getz G (2011). GISTIC2.0 facilitates sensitive and confident localization of the targets of focal somatic copy-number alteration in human cancers. Genome Biol. 12, R41. [PubMed: 21527027]

Northcott PA, Jones DT, Kool M, Robinson GW, Gilbertson RJ, Cho YJ, Pomeroy SL, Korshunov A, Lichter P, Taylor MD, and Pfister SM (2012). Medulloblastomics: the end of the beginning. Nat. Rev. Cancer 12, 818–834. [PubMed: 23175120]

Noushmehr H, Weisenberger DJ, Diefes K, Phillips HS, Pujara K, Berman BP, Pan F, Pelloski CE, Sulman EP, Bhat KP, et al.; Cancer Genome Atlas Research Network (2010). Identification of a CpG island methylator phenotype that defines a distinct subgroup of glioma. Cancer Cell 17, 510–522. [PubMed: 20399149]

Ozawa T, Riester M, Cheng YK, Huse JT, Squatrito M, Helmy K, Charles N, Michor F, and Holland EC (2014). Most human non-GCIMP glioblastoma subtypes evolve from a common proneural-like precursor glioma. Cancer Cell 26, 288–300. [PubMed: 25117714]

Read RD, Cavenee WK, Furnari FB, and Thomas JB (2009). A Drosophila model for EGFR-Ras and PI3K-dependent human glioma. PLoS Genet. 5, e1000374. [PubMed: 19214224]

Shingu T, Ho AL, Yuan L, Zhou X, Dai C, Zheng S, Wang Q, Zhong Y, Chang Q, Horner JW, et al. (2017). Qki deficiency maintains stemness of glioma stem cells in suboptimal environment by downregulating endolysosomal degradation. Nat. Genet. 49, 75–86. [PubMed: 27841882]

Soucy TA, Smith PG, Milhollen MA, Berger AJ, Gavin JM, Adhikari S, Brownell JE, Burke KE, Cardin DP, Critchley S, et al. (2009). An inhibitor of NEDD8-activating enzyme as a new approach to treat cancer. Nature 458, 732–736. [PubMed: 19360080]

Author Manuscript Author Manuscript Author Manuscript Author Manuscript

Sturm D, Bender S, Jones DT, Lichter P, Grill J, Becher O, Hawkins C, Majewski J, Jones C, Costello JF, et al. (2014). Paediatric and adult glioblastoma: multiform (epi)genomic culprits emerge. Nat. Rev. Cancer 14, 92–107. [PubMed: 24457416]

Verhaak RG, Hoadley KA, Purdom E, Wang V, Qi Y, Wilkerson MD, Miller CR, Ding L, Golub T, Mesirov JP, et al.; Cancer Genome Atlas Research Network (2010). Integrated genomic analysis identifies clinically relevant subtypes of glioblastoma characterized by abnormalities in PDGFRA, IDH1, EGFR, and NF1. Cancer Cell 17, 98–110. [PubMed: 20129251]

Wang H, Wang H, Zhang W, Huang HJ, Liao WS, and Fuller GN (2004). Analysis of the activation status of Akt, NFkappaB, and Stat3 in human diffuse gliomas. Lab. Invest. 84, 941–951. [PubMed: 15184909]

Wang Y, Yang J, Zheng H, Tomasek GJ, Zhang P, McKeever PE, Lee EY, and Zhu Y (2009). Expression of mutant p53 proteins implicates a lineage relationship between neural stem cells and malignant astrocytic glioma in a murine model. Cancer Cell 15, 514–526. [PubMed: 19477430]

Wang Y, Kim E, Wang X, Novitch BG, Yoshikawa K, Chang LS, and Zhu Y (2012). ERK inhibition rescues defects in fate specification of Nf1-deficient neural progenitors and brain abnormalities. Cell 150, 816–830. [PubMed: 22901811]

Wu SH, Bi JF, Cloughesy T, Cavenee WK, and Mischel PS (2014). Emerging function of mTORC2 as a core regulator in glioblastoma: metabolic reprogramming and drug resistance. Cancer Biol. Med. 11, 255–263. [PubMed: 25610711]

Zheng H, Ying H, Yan H, Kimmelman AC, Hiller DJ, Chen AJ, Perry SR, Tonon G, Chu GC, Ding Z, et al. (2008). p53 and Pten control neural and glioma stem/progenitor cell renewal and differentiation. Nature 455,1129–1133. [PubMed: 18948956]

Zhu Y, Guignard F, Zhao D, Liu L, Burns DK, Mason RP, Messing A, and Parada LF (2005). Early inactivation of p53 tumor suppressor gene cooperating with NF1 loss induces malignant astrocytoma. Cancer Cell 8, 119–130. [PubMed: 16098465]

Highlights

- *p53*-mutant-driven gliomas acquire chromosomal alterations of adult primary GBM

- Rictor/mTORC2 loss delays glioma formation and prolongs survival

- Rictor deletion with p53 loss promotes SHH-MB formation from GCPs

- Low Rictor expression is associated with poor survival of human pediatric SHH-MBs
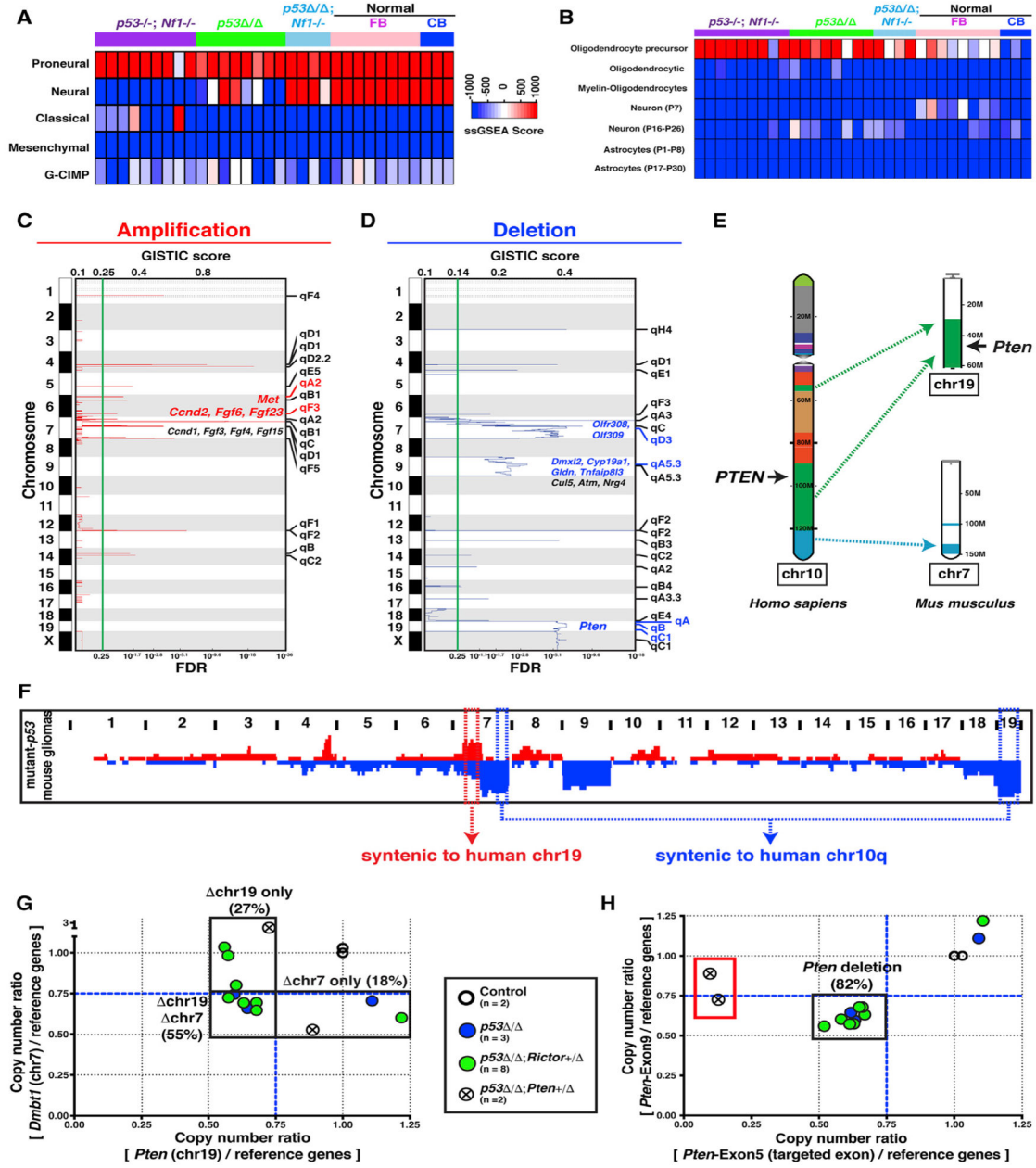
Figure 1. *p53*-Mutant Malignant Gliomas Exhibit Unique Genomic Alterations Consistent with Human Primary GBMs

(A and B) Gene expression profiles of the *p53*-mutant-driven malignant gliomas with or without targeted *Nf1* deletions are compared to those of human GBM subgroups (A) and different cell lineages in the brain (B). High single-sample gene set enrichment analysis (ssGSEA) score (red) indicates strong similarity, while low scores (blue) indicate dissimilarity. FB, forebrain; CB, cerebellum.

(C and D) The GISTIC method was used to detect both local and broad CNAs in 23 GEM malignant gliomas. GISTIC scores and FDRs are indicated in the upper and lower parts of the × axes, respectively. Chromosomal regions with amplification peaks (C) or deletion

peaks (D) are listed. Some frequently amplified and deleted genes in both GEM malignant gliomas and *TP53* mutant human GBMs are highlighted in red and blue, respectively.

(E) Synteny map comparing the human chr10q with the mouse chr19 and chr7.

(F) Genome plot displaying the frequencies of the copy-number gains (red) and losses (blue) in these 23 GEM malignant gliomas. Segments of the mouse chr19 and chr7 (syntenic to human chr10q) and mouse chr7 (syntenic to human chr19) are indicated with dashed-line boxes.

(G and H) qPCR experiments for CNA analysis were performed in an additional cohort of GEM malignant gliomas. Plots show the ratio of copy number of *Pten* (gene on chr10) and *Dmbt1* (gene on chr7) (G) and two distinct exons of the *Pten* gene (H) in tumor samples separately. Black boxes indicate the specific deletion events, and the red box indicates malignant gliomas, where *Pten* exon 5 (but not exon 9) is deleted by the Cre/LoxP strategy. See also Figure S1 and Table S1.
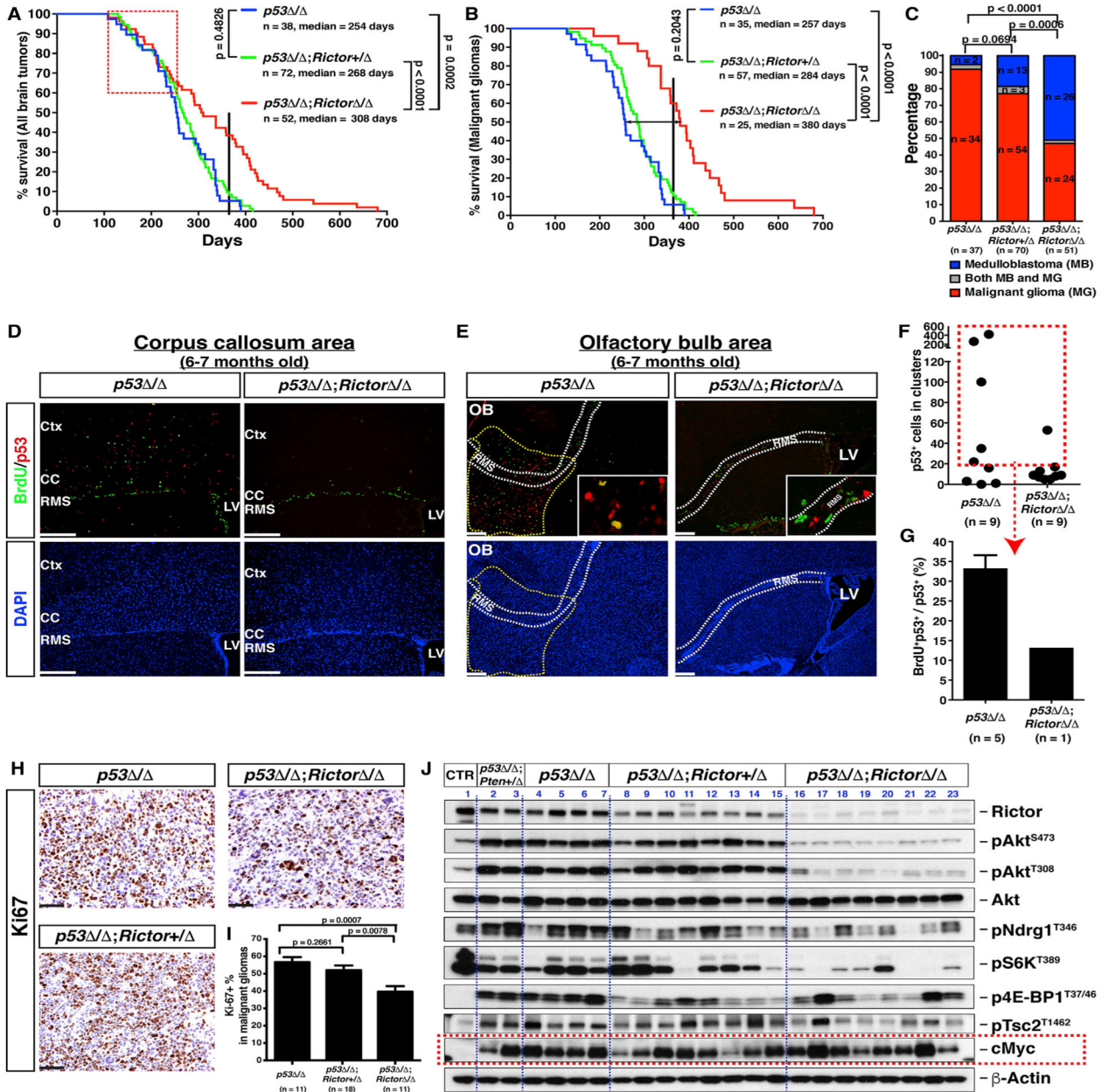
Figure 2. *Rictor* Deletion Inhibits *p53*-Mutant-Driven Malignant Glioma Formation

(A and B) Kaplan-Meier survival curves of mice sacrificed because of end-stage brain tumors (A) or end-stage malignant gliomas (B) in three models. Black dashed line indicates 1 year. Red dashed-line box in (A) indicates a comparable survival rate.

(C) The frequency of malignant gliomas and MBs.

(D and E) Mutant mice at age 6–7 months were injected with BrdU for proliferation assay. Expansion of the glioma precursor population around the corpus callosum (D) and rostral migratory stream (E) is illustrated by p53 and BrdU staining. Yellow dashed-line area indicates the p53 $^{5-6+}$ cluster. Ctx, cerebral cortex; CC, corpus callosum; OB, olfactory bulb; RMS, rostral migratory stream; LV, lateral ventricle.

(F and G) The total number of the p53 $^{5–6+}$ cells scattered and/or clustered outside the germinal zone was quantified in *p53* $^{5–6/~5–6}$ and *p53* $^{5–6/~5–6}$*Rictor* $^{/}$ mice (F). The percentage of the proliferating p53 $^{5–6+}$ cells was calculated using the samples that have 20 p53 $^{5–6+}$ cells (G).

(H and I) Tumor cell proliferation in malignant gliomas based on Ki67 staining is shown in (H) and quantified in (I).

(J) Western blot analyses of malignant gliomas from different GEM models. Normal cortical tissue was used as control (CTR), and two malignant gliomas that harbored *p53* and *Pten* mutations (described in Figure S3D) were included.

All of the quantification data are presented as means ± SEMs. The Mantel-Cox (log-rank) test was used to compare the survival curves (A and B). Two-tailed Fisher's exact test was used to compare the groups (C and G). Scale bars: 250 µm (D and E) and 50 µm (H). See also Figure S2.
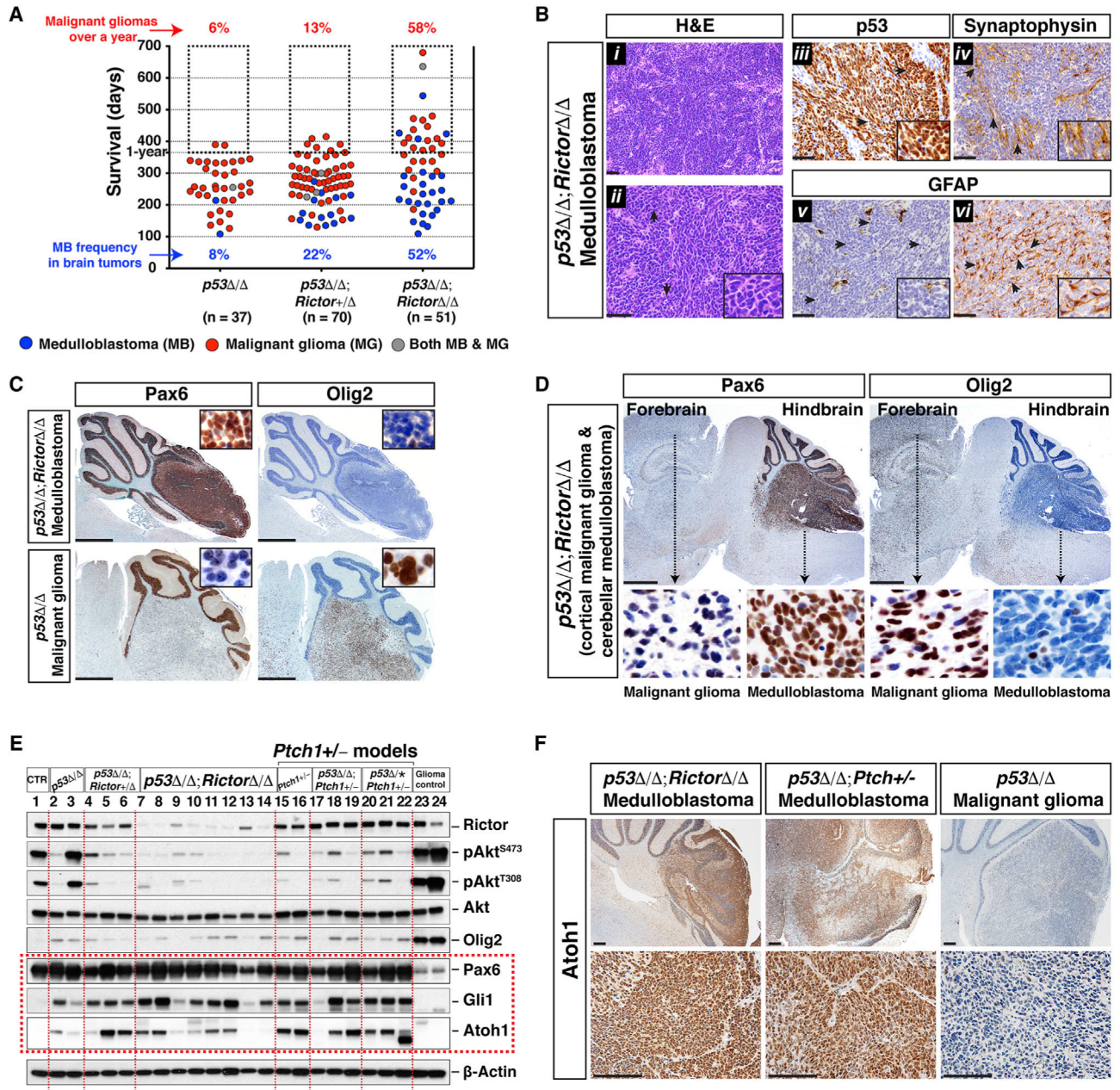
Figure 3. *Rictor* Deletion Promotes *p53*-Mutant-Driven Medulloblastoma Formation

(A) Scatterplot representation of malignant gliomas and MBs along with their corresponding survival rates in three GEM models.

(B) Histopathological features of the *p53* $^{5-6/}$ $^{5-6}$*Rictor* $^{/}$ MBs. H&E staining shows the dense tumor (*i*) with carrot-shaped nuclei, apoptotic cells, and nuclear moldings (*ii*). Tumors were immunoreactive to p53 (*iii*) and synaptophysin (*iv*) antibodies. Tumor areas with GFAP$^−$ (*v*) and GFAP$^+$ (*vi*) are shown. Insets are higher magnification images.

(C) Immunohistochemical analysis of Pax6 and Olig2 expression in a *p53* *5–6/* *5–6Rictor* */*
MB and a *p53* *5–6/* *5–6* malignant glioma located in the cerebellum. Insets show higher
magnification views.

(D) Pax6 and Olig2 staining in adjacent sections of a *p53* *5–6/* *5–6Rictor* */* brain with a
malignant glioma in the forebrain and an MB in the cerebellum.

(E) Western blot analysis of MBs from different GEM models. WT cerebellar tissue (CTR)
and two malignant glioma samples (last two lanes) are included. SHH-MB-related markers
are framed with a red dashed-line box.

(F) Immunohistochemical analysis of Atoh1 expression in MBs and malignant glioma
located in the cerebellum.

Scale bars: 50 μm (B), 1 mm (C and D), and 250 μm (F).

See also Figure S3.
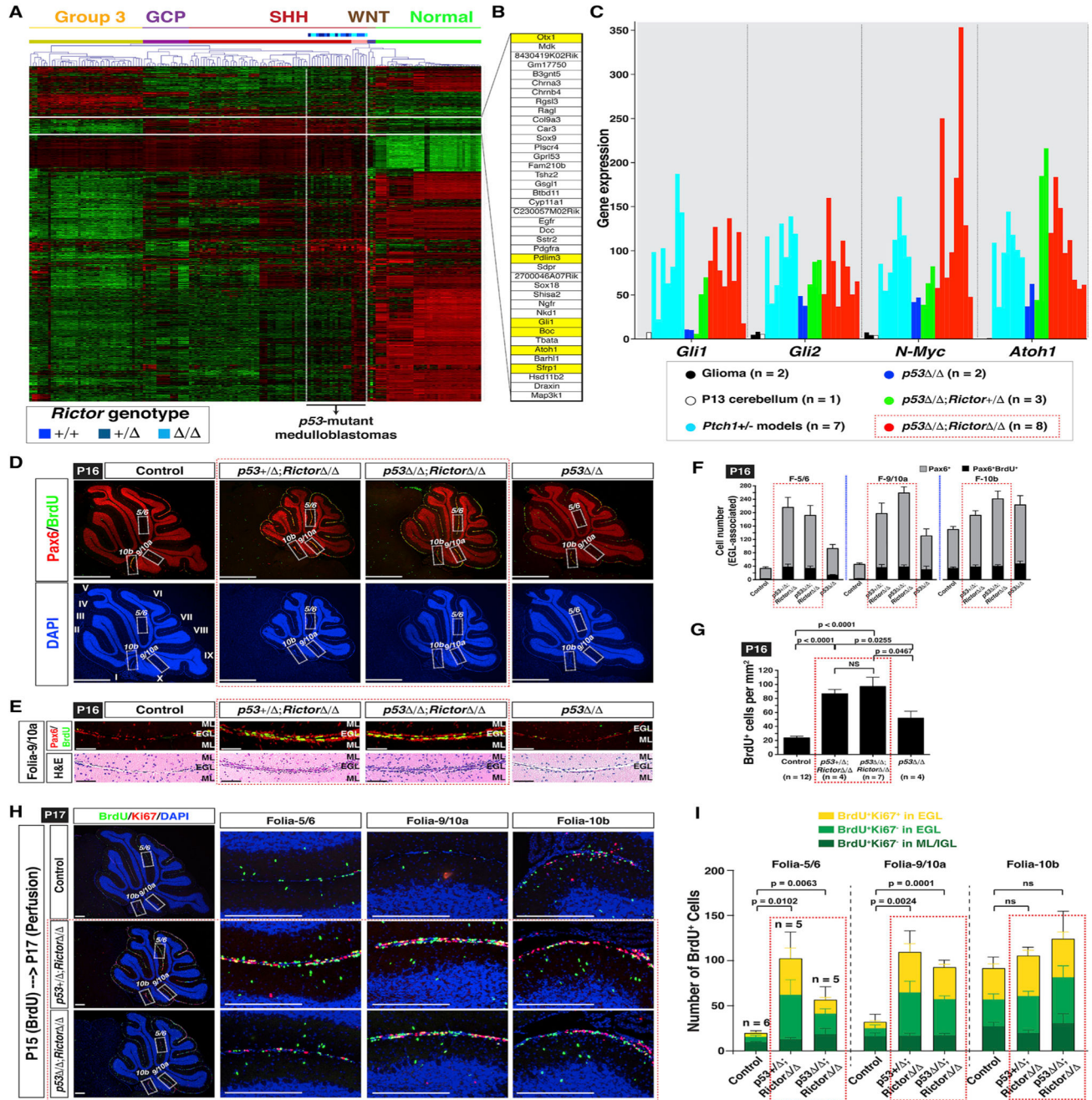
Figure 4. *Rictor* Deletion Promotes SHH-MB Formation by Prolonging the Proliferation of Granule Cell Precursors

(A and B) Microarray analysis of genome-wide expression profiles of the *p53*-mutant-driven MBs in comparison with normal cerebellum and previously published GEM models of WNT, SHH, and group 3 MBs. An area containing the genes specifically upregulated in the SHH-MBs and GCPs is highlighted with the horizontal white box (A). The genes in this area are listed in (B) and the important ones are highlighted in yellow.

(C) qPCR experiments were performed using cDNAs from *p53* [5–6]-driven MBs in comparison with the *Ptch1*^{+/−} models. Two malignant glioma samples and one P13 normal cerebellar tissue were used as negative controls.

(D–G) Control and mutant mice at P16 were injected with BrdU and analyzed 2 hr later. The overall cerebellar structure along with the Pax6^{+} cells and BrdU^{+} proliferating cells were examined. Each folium ("F") is labeled with Roman numerals (D). White frames indicate three areas (F-5/6, F-9/10a, and F-10b) that were subjected to further analysis. Two types of *Rictor* mutant mice are highlighted by red dashed-line boxes. Higher magnification of F-9/10a regions in (D), and corresponding H&E staining is shown (E). Pax6^{+} cells and proliferating BrdU[+]Pax6^{+} cells in the EGL-associated areas were quantified in three folia of P16 control and mutant cerebella (F). The total number of BrdU^{+} proliferating cells per unit area (mm^2) was calculated for control and mutant cerebella individually (G).

(H and I) Cell-cycle analysis was performed by injecting the mice with BrdU once at P15 and analyzing at P17. Two types of *Rictor* mutant mice are highlighted by red dashed-line boxes. (H) The cells proliferating at P15 were labeled with BrdU upon injection. Those subsequently exiting the cell cycle at P17 were labeled BrdU[+]Ki67^{−} (green), and those remained or re-entered cell cycle were labeled BrdU[+]Ki67^{+} (yellow). Higher magnification view of the EGL cells in F-5/6, F-9/10a, and F-10b are shown. (I) The number of BrdU^{+} cells in EGL, ML, and IGL are quantified. The distribution of each type of BrdU^{+} cells is shown with bar graphs. The p values for the comparisons of BrdU[+]Ki67^{+} cells in EGL (yellow bars) are shown. Additional comparisons are listed in Figure S4F. All of the quantification data are presented as means ± SEMs. Unpaired Student's t test was used to compare the groups statistically. Scale bars: 1 mm (D), 100 μm (E), and 250 μm (H). EGL, external granular layer; IGL, internal granular layer; ML, molecular layer.

See also Figure S4.
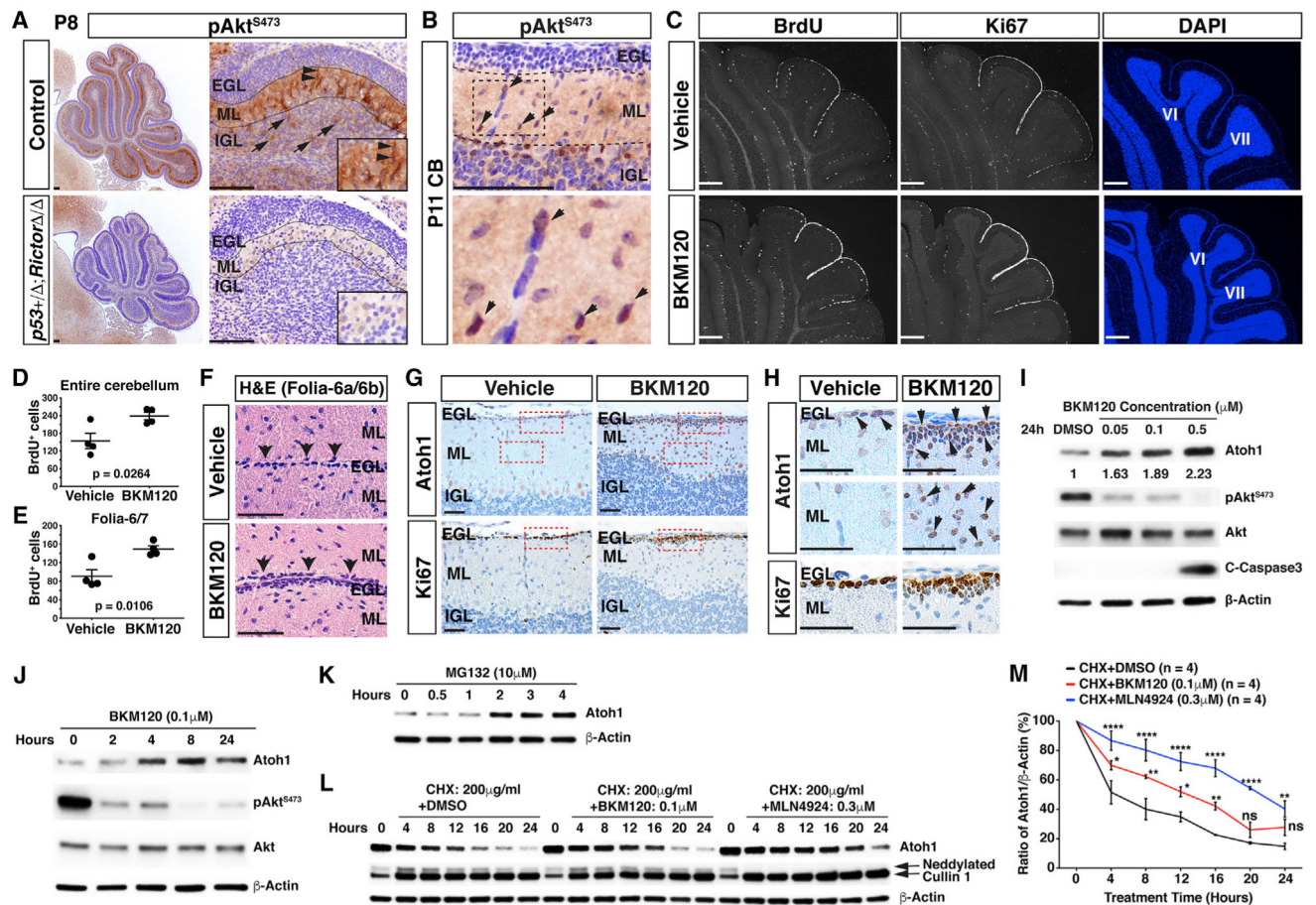
Figure 5. Pharmacological Inhibition of Akt Signaling Delays Granule Cell Precursor Differentiation by Blocking Atoh1 Degradation

(A and B) pAkt^{S473} immunohistochemical staining in WT and $p53^{+/\Delta}$ $^{5-6}Rictor^{\Delta/\Delta}$ cerebella at P8 (A) and in WT at P11 (B). Arrows indicate the differentiated neurons with robust pAkt^{S473} expression in IGL. Arrowheads indicate the migrating granule cells with high pAkt^{S473} expression in ML.

(C–H) WT mice were treated with vehicle or BKM120 (10 μM) from P8 to P16. Analyses were performed at P16. (C) Representative images of cerebellar sections in vehicle- or BKM120-treated WT mice. BrdU and Ki67 staining are shown in grayscale; DAPI is shown in blue. F-6 and F-7 are indicated with Roman numerals.

(D and E) Total BrdU$^+$ cell number was quantified in the entire EGL (D) or only in F-6 and F-7 (E) of the treated mice. (F) Representative H&E staining of cerebella from vehicle- or BKM120-treated mice. Higher magnification images of marked areas in F-6a/−6b are shown. Arrowheads indicate the retained cells in EGL. (G and H) Atoh1 and Ki67 staining in adjacent sections of vehicle- and BKM120-treated WT cerebella. F-6 is shown. Areas outlined in red dashed lines are shown in higher magnifications in (H). Arrowheads point toward Atoh1$^+$ cells.

(I–L) p53 $^{5-6/5-6}$ medulloblastoma cell line was treated as indicated, and cells were collected and subjected to western blot analysis. (I) Cells were treated with DMSO or

different doses of BKM120 as indicated for 24 hr. The band density of Atoh1 was quantified and the ratio of Atoh1/β-actin was calculated. (J and K) Cells were treated with BKM120 (0.1 μM [J]) or MG132 (10 μM [K]), as indicated. (L) Cells were treated with 200 μg/mL cycloheximide (CHX) together with DMSO, BKM120, or MLN4924, as indicated. One representative result (of four) is shown.

(M) The band density of Atoh1 and β-actin were quantified for each repeated experiment in (L). The percent ratio of Atoh1/β-actin was calculated accordingly and graphed. $*p < 0.05$, $**p < 0.01$, $***p < 0.001$, $****p < 0.0001$.**** All of the quantification data are presented as means ± SEMs. Unpaired Student's t test was used to compare the groups in (D) and (E). Two-way ANOVA was performed in (M). Scale bars: 100 μm (A and B), 250 μm (C), and 50 μm (F–H). EGL, external granular layer; IGL, internal granular layer; ML, molecular layer. See also Figure S5.
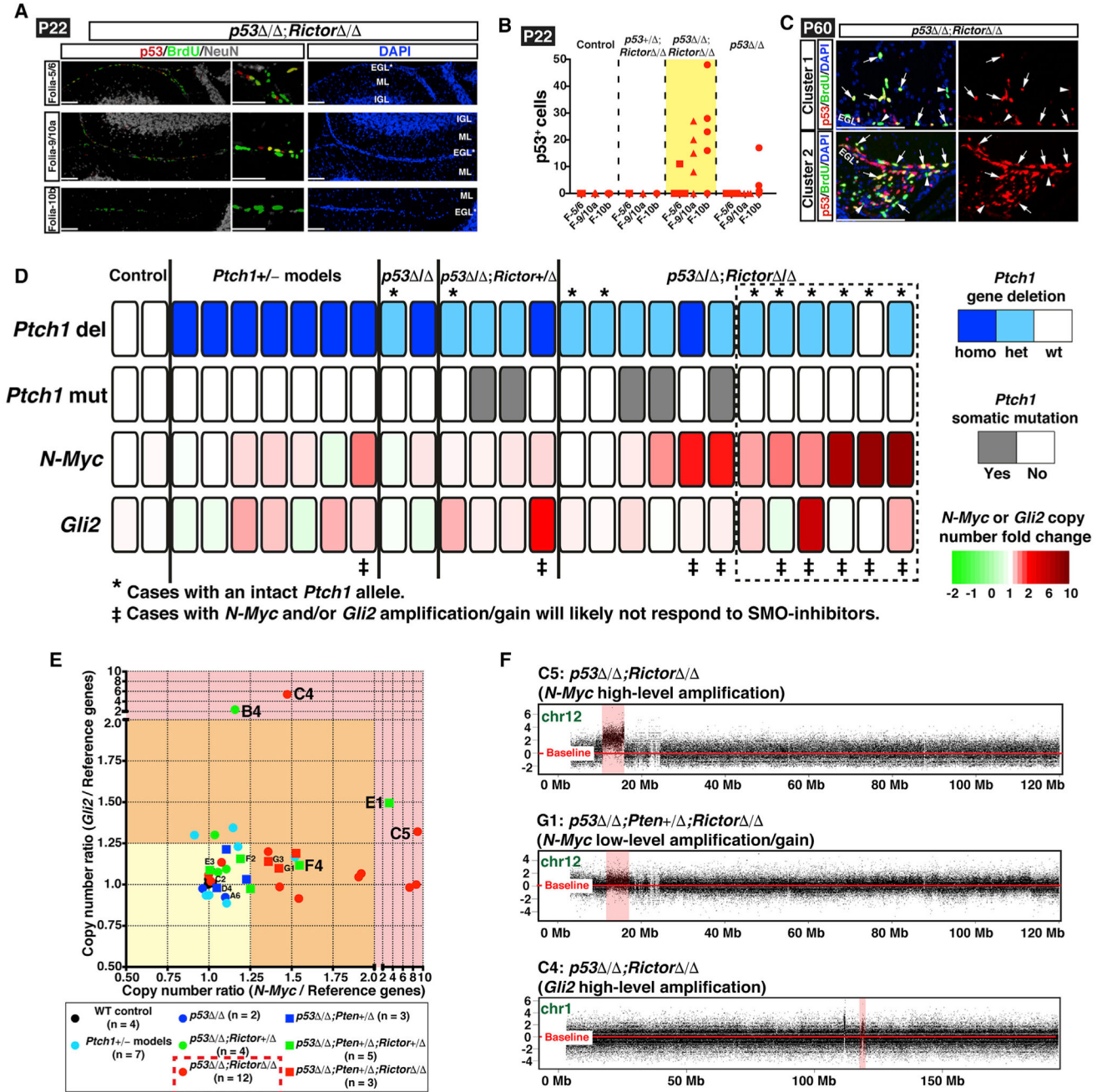
Figure 6. *p53*-Mutant-Driven MBs Share Critical Features of *TP53* Mutant SHH-MBs in Humans

(A) Proliferating p53[5–6+] cells in multiple folia in *p53[5–6/ 5–6]Rictor[/]* cerebella at P22. NeuN staining labels the differentiated IGL cells.

(B) The total number of p53[5–6+] cells in three different folia from P22 WT and mutant mice is shown.

(C) Clustered BrdU[+]p53[5–6+] cells in *p53[–6/ 5–6]Rictor[/]* cerebella at P60. Arrows indicate BrdU[+]p53[5–6+] cells; arrowheads indicate BrdU[+]p53^{−} cells.

(D) SHH pathway alterations in SHH-MBs from different GEM models.

(E) Analysis of CNAs in *N-Myc* and *Gli2* genes in a bigger pool of MB samples. Copy-number ratios   1.25 were considered low-level amplifications/gains (orange area), ratios >2 were considered high-level amplifications (light red area).

(F) Amplified chromosomal regions containing *N-Myc* and *Gli2* genes (red) detected by low-coverage whole-genome sequencing (lcWGS). This parameter is shown as a ratio of tumor versus control tissue. Baseline is shown with a red line across the plots.

Scale bars: 50 μm (A and C). EGL, external granular layer; IGL, internal granular layer; ML, molecular layer.

See also Figures S6 and S7.
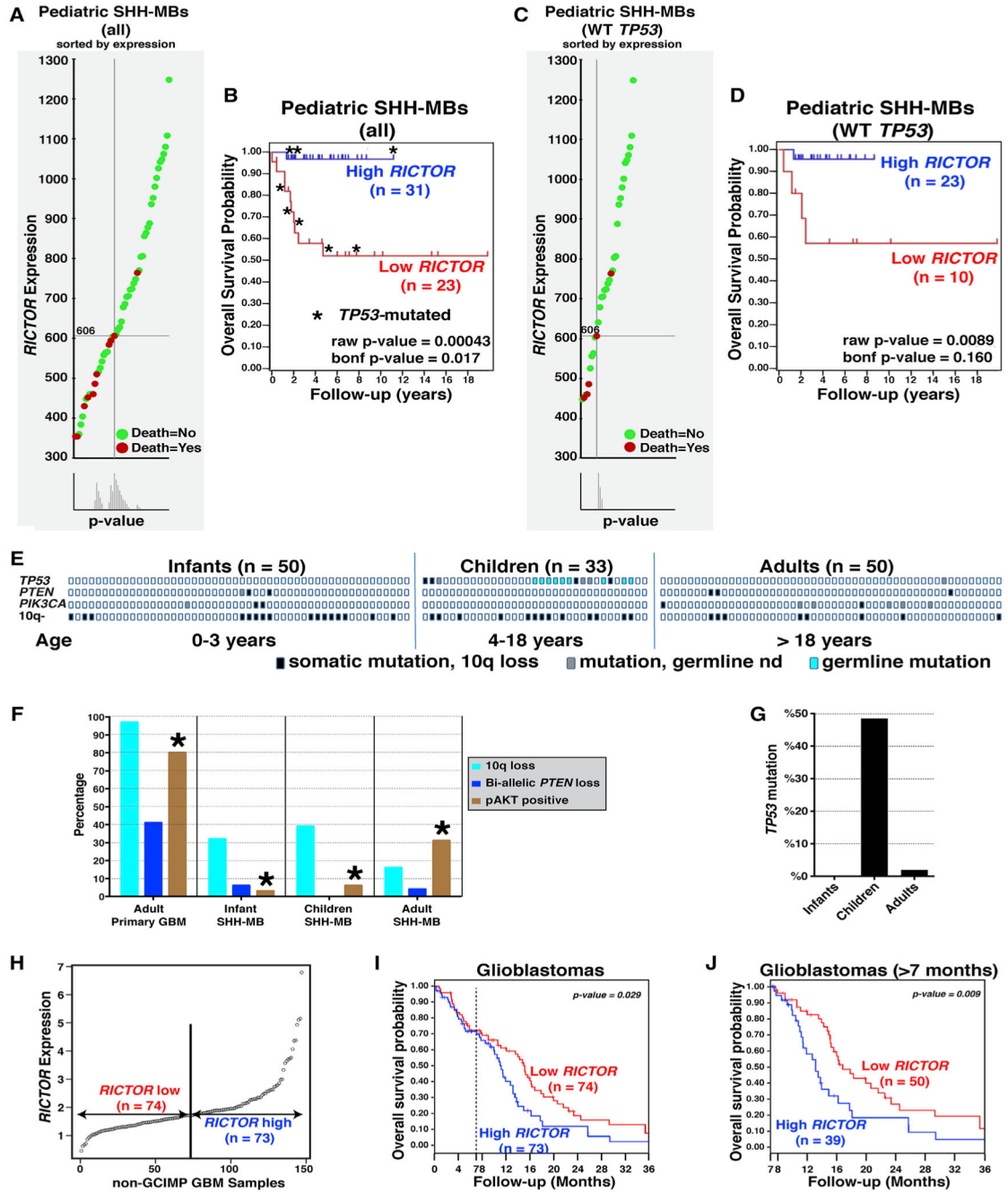
Figure 7. *RICTOR* Expression Is Correlated with Opposite Clinical Outcomes in Adult GBMs and Pediatric SHH-MBs

(A-D) Scatterplot distribution of *RICTOR* gene expression among all pediatric SHH-MBs (A) or pediatric SHH-MBs with WT *TP53* only (C). Patients who succumbed to the disease are indicated with red dots, while the survivors at the time of analysis are shown with green dots. The survival analysis for both groups is shown in (B) and (D). Tumors with detected *TP53* mutations are indicated with asterisks in (B).

(E) Distribution of *TP53, PTEN*, and *PIK3CA* gene mutations and chr10q loss in SHH-MBs among the three age subgroups.

(F) The frequencies of 10q loss, biallelic *PTEN* inactivation, and pAKT positivity (* derived from two previous studies) are compared between adult primary GBMs and SHH-MBs.

(G) Percentages of *TP53* mutations within each age subgroup of SHH-MBs.

(H) Scatterplot representation of *RICTOR* expression among human primary GBM samples.

(I and J) Overall survival probability of the GBM patients based on their *RICTOR* expression. The whole cohort is shown in (I); patients with survival >7 months are shown in (J).

Multiple corrected log-rank tests between pairs of groups are used for comparisons of survival curves in (B), (D), (I), and (J). The individual datasets are initially scanned to find the cutoff in expression that results in the lowest p value between high and low expression values.

See also Figure S8.

KEY RESOURCES TABLE

REAGENT or RESOURCE	SOURCE	IDENTIFIER
Antibodies		
Rabbit anti-p53	Leica	P53-CM5P-L
Rabbit anti-Olig2	Millipore	AB9610
Rabbit anti-GFAP	Dako	Z0334
Rabbit anti-Synaptophysin	Covance	MMS-618R
Rabbit anti-Pax6	Covance	PRB-278p
Rabbit anti-Ki67	Abcam	ab15580
Rabbit anti-pAkt^{S473}	Cell Signaling	4060L
Rabbit anti-Atoh1	Dr. Jane Johnson from UT Southwestern	N/A
Mouse anti-Atoh1	Abcam	ab27667
Mouse anti-Atoh1	Developmental Studies Hybridoma Bank	N/A
Rat anti-BrdU	Abcam	ab6326
Mouse anti-Ascl1/Mash1	BD PharMingen	556604
Mouse anti-Nestin	Millipore	MAB353
Goat anti-Sox2	Santa Cruz Biotech	sc-17320
Mouse anti-Calbindin	Sigma-Aldrich	C9848
Mouse anti-NeuN	Millipore	MAB377
Alexa Fluor 488	Invitrogen, Life Technologies	A11004; A11034
Alexa Fluor 555	Invitrogen, Life Technologies	A21429; A21424
Alexa Fluor 647	Invitrogen, Life Technologies	A31571; A21236; A21247; A21245
Alexa Fluor 555-conjugated streptavidin	Thermo Fisher Scientific	S-32355
Rabbit anti-pAkt^{T308}	Cell Signaling	2965S
Rabbit anti-Akt	Cell Signaling	9272S
Rabbit anti-pNDRG1^{T346}	Cell Signaling	5482S
Rabbit anti-Pten	Cell Signaling	9559S
Rabbit anti-Rictor	Dr. D. Fingar from University of Michigan	N/A
Rabbit anti-mTOR	Cell Signaling	2983S
Mouse anti-β-Actin	Sigma-Aldrich	A5316
Rabbit anti-pS6K^{T389}	Cell Signaling	9234S
Rabbit anti-p4E-BP1$^{T37/46}$	Cell Signaling	9459S
Rabbit anti-pTSC2^{T1462}	Cell Signaling	8350S
Rabbit anti-pS6$^{S240/244}$	Cell Signaling	5364S
Rabbit anti-S6	Cell Signaling	2217S
Rabbit anti-cMyc	Cell Signaling	5605S
Rabbit anti-pErk1/2$^{T202/Ty204}$	Cell Signaling	9101S
Rabbit anti-Erk1/2	Cell Signaling	9102L
Rabbit anti-pGSK-3β^{S9}	Cell Signaling	5558S

REAGENT or RESOURCE	SOURCE	IDENTIFIER
Mouse anti-P120	BD Biosciences	610040
Rabbit anti-Gli1	Cell Signaling	2534S
Rabbit anti-Atoh1	Abcam	ab168374
Cleaved-Caspase3	Cell Signaling	9661S
Mouse anti-Cul-1	Santa Cruz	sc-17775
HRP-conjugated secondary antibodies	BioRad	1706515; 1706516
Chemicals, Peptides, and Recombinant Proteins		
BKM120	Selleckchem	S2247
Vehicle	Sigma-Aldrich	C5135
PEG400	Sigma-Aldrich	202398
KaryoMAX Colcemid solution	GIBCO, Life Technologies	15212012
KaryoMAX Potassium Chloride Solution	GIBCO, Life Technologies	10575-090
Cycloheximide	Sigma-Aldrich	C7698-1G
MLN4924	Selleckchem	S7109
MG132	Selleckchem	S2619
Critical Commercial Assays		
CellTiter-Glo Luminescent Cell Viability Assay	Promega	G7572
QuantiTect Reverse Transcription Kit	QIAGEN	205313
AllPrep DNA/RNA Mini Kit	QIAGEN	80204
SYBR Select Master Mix	Thermo Fisher Scientific	4472908
Deposited Data		
Gene expression	GEO	GSE78895
Experimental Models: Cell Lines		
Established primary brain tumor cell lines from GEM models in this study	This paper	N/A
Experimental Models: Organisms/Strains		
hGFAP-cre	Wang et al., 2009	N/A
$p53^{E5-6flox}$	Wang et al., 2009	N/A
$Rictor^{flox}$	Magee et al., 2012	N/A
$Pten^{flox}$	Zheng et al., 2008	N/A
$Ptch1^{+/-}$	Frappart et al., 2009	N/A
Oligonucleotides		
Primers for genotyping PCR, gene expression and copy number analysis, see Table S2	This paper	N/A
Software and Algorithms		

REAGENT or RESOURCE	SOURCE	IDENTIFIER
GISTIC	Mermel et al., 2011	https://software.broadinstitute.org/software/cprg/?q=node/31
Integrative Genomics Viewer (IGV)	N/A	https://software.broadinstitute.org/software/igv/
ImageJ (Version 1.52c)	N/A	https://imagej.nih.gov/ij/